

SLAC - PUB - 4419
September 1987
(E)

DESIGN AND PERFORMANCE OF
• A DOUBLE-ARM 180° SPECTROMETER SYSTEM FOR
MAGNETIC ELECTRON SCATTERING FROM DEUTERIUM*

A. T. KATRAMATOU, G. G. PETRATOS, R. G. ARNOLD, P. E. BOSTED

*Department of Physics, The American University
Washington, D.C. 20016*

R. L. EISELE, R. A. GEARHART

*Stanford Linear Accelerator Center
Stanford University, Stanford, CA 94305*

ABSTRACT

The design and operation of a double-arm 180° spectrometer system for elastic and inelastic electron scattering from deuterium is described. The system consisted of a chicane of dipole magnets to transport an incident electron beam to a target, an upstream QQQDD spectrometer with a bend angle of 65° to analyze backscattered electrons, a downstream QQQDDDD spectrometer with a bend angle of 66° to detect recoil particles produced at 0°, and a moveable beam dump. The large acceptance of the system allowed measurements of the deuteron magnetic elastic $B(Q^2)$ and inelastic $W_1(\nu, Q^2)$ structure functions at high momentum transfers. The performance is compared to the predictions of a Monte Carlo simulation program.

Submitted to *Nuclear Instruments and Methods*

* Work supported in part by the Department of Energy, contract DOE-AC03-76SF00515 (SLAC) and by National Science Foundation, grant PHY85-10549 (AU).

1. INTRODUCTION

This paper describes the design, operation and performance of a double-arm large acceptance spectrometer system for magnetic electron scattering from deuterium. The upstream arm was arranged to focus and momentum analyze electrons scattered near 180° to a set of detectors. A portion of this arm also transmitted the primary beam to the target. The downstream arm transported nuclei recoiling near 0° to another set of detectors, as well as directing the transmitted electron beam to a water-cooled dump. This was the first system ever built for measuring 180° electron scattering in which the recoil particles are detected in coincidence with the scattered electrons.

The apparatus was installed in End Station A (ESA) at the Stanford Linear Accelerator Center (SLAC) for experiment NE4.^[1] The high intensity electron beam from the Nuclear Physics Injector (NPI)^[2] was used to make cross section measurements for elastic, threshold inelastic, and quasi-elastic electron scattering from deuterium. These measurements extended our knowledge of the deuteron magnetic structure functions $B(Q^2)$ and $W_1(\nu, Q^2)$ and allowed an important comparison with the previously measured forward angle structure functions $A(Q^2)$ and $W_2(\nu, Q^2)$ at high values of the four momentum transfer squared Q^2 .

The need for a complicated spectrometer system was dictated by several factors. The principal factor was that the ratio $B(Q^2)/A(Q^2)$ was predicted to be small (0.05 to 0.005) in the Q^2 region of interest 1 to 5 (GeV/c)². To enhance the contribution from the magnetic term $B(Q^2)$, the electron scattering angle needed to be close to 180° where the contribution from $A(Q^2)$ vanishes. This can be seen from the equation for elastic scattering:

$$\frac{d\sigma}{d\Omega} = \frac{\alpha^2 E'}{4E^3 \sin^4 \frac{\Theta}{2}} \left[A(Q^2) \cos^2 \frac{\Theta}{2} + B(Q^2) \sin^2 \frac{\Theta}{2} \right] \quad (1.1)$$

where α is the fine structure constant, Θ is the electron scattering angle, and E and E' are the incident and final electron energies. The selection of 180° as

the electron scattering angle also resulted in measurements of W_1 only, with no contributions from W_2 , as can be seen from the equation for inelastic scattering:

$$\frac{d^2\sigma}{d\Omega dE'} = \frac{\alpha^2}{4E^2 \sin^4 \frac{\Theta}{2}} \left[W_2(\nu, Q^2) \cos^2 \frac{\Theta}{2} + 2W_1(\nu, Q^2) \sin^2 \frac{\Theta}{2} \right] \quad (1.2)$$

where ν is the energy transfer $E - E'$.

The elastic cross section falls rapidly with Q^2 , and was predicted to be as small as 10^{-41} cm²/sr at $Q^2 = 5$ (GeV/c)². Therefore, an electron spectrometer with the largest practical solid angle and the longest possible targets were needed to maintain reasonable counting rates. The design goals were for a solid angle on the order of 20 msr using liquid deuterium targets between 10 and 40 cm in length.

The small binding energy of the deuteron (2.2 MeV) and the poor resolution caused by the energy losses of the incident and back-scattered electrons in thick targets would have made it impossible to distinguish elastic electron-deuteron scattering events from inelastic scattering events by detecting electrons only. Therefore, the deuterons recoiling near 0° were detected in coincidence using the downstream arm. This arm had to be capable of spatially separating the positively charged deuterons from the degraded and multiply scattered electron beam and directing the beam to a well-shielded dump. It also needed enough bending power to sweep away all the low energy charged particle background. Our design goal was to have the acceptance for the recoil spectrometer be large and completely overlap that of the electron spectrometer for elastic coincidence kinematics. The purpose of this requirement was to facilitate the calculation of radiative corrections and minimize the errors in the calculations of the double-arm solid angles.

A large momentum acceptance for the electron spectrometer was desirable to minimize the data taking time for the single-arm inelastic measurements. A final constraint on the overall design parameters came from the desire to use

double-arm electron-proton elastic scattering for momentum calibration and to check the calculations of double-arm solid angles. The allowed range in deflection angles in the primary beam transport and beam dump lines were increased to allow ep calibrations to be made over a large momentum range.

An overview of the entire system is given in Section 2. In Section 3 the hardware and beam optics design is described in detail. The calibration of the apparatus is detailed in Section 4 while the performance compared to the Monte Carlo predictions is made in Section 5. Concluding remarks are given in Section 6.

2. OVERVIEW OF THE SYSTEM

Figure 1 shows the entire spectrometer system. The electron arm and beam transport chicane are shown in more detail in Figure 2. As in other 180° systems,^[3,4] there were two overlapping channels on the electron side: one for the incident beam and one for the back-scattered electrons. The beam, after exiting the SLAC beam switchyard into End Station A, traveled through the chicane of bending magnets B1-B2-B3 and along the magnetic axis of the quadrupole triplet Q1-Q2-Q3 to impinge on the target. The back-scattered electrons were focused by the same triplet and transported through the bending magnets B3 and B4 to a detection system. This quadrupole triplet provided the large gathering power for the relatively low energy back-scattered electrons needed to achieve a large solid angle while having little effect on the transported incident beam. For a thin target, the solid angle was 22.5 msr averaged over a momentum acceptance range of $\pm 4\%$. The momentum and scattering angle resolutions were typically $\pm 0.4\%$ and $\pm 8 \text{ mr}$.

The ratio of incident to scattered electron momenta changed with the desired kinematics for both elastic and inelastic scattering. Therefore the beam deflection angle in magnet B3 also changed. The bending magnets B1 and B2 served only as primary beam transport elements. Magnet B2 was placed symmetrically along the beam direction with respect to B1 and B3, and the B2 deflection angle θ_{B2} was

twice the deflection angle θ_{B1} in magnets B1 and B3. The horizontal position of B2 and the bend angles θ_{B1} and θ_{B2} were adjusted as necessary to accommodate specific kinematic settings.

On the recoil side, shown in more detail in Figure 3, there were also two overlapping channels: one for the recoil nuclei and one for the transmitted beam. Both the electrons and deuterons passed through the quadrupole triplet Q4-Q5-Q6 before entering the bending magnet B5, which played the crucial role of separating the recoil particles from the electrons. The transmitted electron beam (degraded by radiation, ionization, and multiple scattering) was deflected towards a water-cooled dump. The positively charged recoil particles were bent in the other direction and transported through three additional bending magnets B6-B7-B8 to a set of detectors.

The focusing strengths of the quadrupole triplet Q4-Q5-Q6 were chosen to maximize the transmission of nuclei through the recoil spectrometer, while simultaneously achieving an acceptable beam spot size on the dump, taking into account the angular and momentum spread in both channels from kinematics and interactions at the target. For radiationless elastic scattering above $Q^2 = 1$ (GeV/c)², almost every deuteron associated with an electron detected in the electron spectrometer was transmitted to the recoil detectors for a wide range of target lengths. For a thin target, the solid angle of the recoil spectrometer was 5.9 msr averaged over a momentum acceptance range of 2.0%. The momentum resolution was typically $\pm 0.3\%$ and the resolution in the deuteron recoil angle was ± 9 mr.

The ratio of the incident electron momentum to the recoil deuteron or proton momentum varies with kinematics. Since the recoil angle was fixed, this caused the beam deflection in magnet B5 to change. Fortunately, in the kinematic range considered, this variation was only a few degrees. This dictated the need for a movable dump placed as close to the magnet B5 as the shielding requirements allowed. The large distances between the detectors and sources of direct

background at the target and the beam dump allowed sufficient space for protective layers of concrete and iron shielding blocks.

The detection system of the electron side consisted of a set of multi-wire proportional chambers (MWPCs) for track reconstruction, two planes of scintillation counters for triggering and fast timing, a gas threshold Čerenkov counter and a total absorption shower counter for particle identification. On the recoil side there was a set of multi-wire proportional chambers and two segmented planes of plastic scintillators with a separation of 8 meters for single- and double-arm time-of-flight measurements.

3. DESIGN OF THE SYSTEM

The detailed optimization of the spectrometers was carried out using several tools. The computer code TRANSPORT^[5] was used to evaluate first- and second-order matrix elements for specific configurations, while the computer code TURTLE^[6] was used to evaluate solid angles using first- and second-order matrix elements. For the optimization of specific design parameters (field strengths, drift distances, bend angles, etc.), the TRANSPORT and TURTLE programs were found to be too slow, so a simple thin lens model computer program was developed to evaluate first-order matrix elements and solid angles and determine resolutions. The details of this computer model are given below. The final optimization of some of the system parameters was made using a ray-tracing Monte Carlo program^[7] that used measured magnetic field maps to transport particles through the magnets and took into account the effects of multiple scattering and ionization and radiative energy loss.

The spectrometer system was designed to utilize existing surplus magnets due to budget constraints. Magnets were chosen to achieve the largest possible solid angle for the momenta ranges of the double-arm ed kinematics. To achieve this goal, quadrupoles of short length, high gradient, and large aperture were needed, as were bending magnets with vertical gaps comparable to the apertures

of the quadrupoles. As a rule, the acceptance of a spectrometer is inversely proportional to its length. For this reason the drift lengths were generally kept as short as possible consistent with the moderate resolution requirements.

The next sub-sections give details on the thin lens model and the detailed designs of the electron spectrometer, beam transport system, recoil spectrometer, and beam dump. Additional details can be found in Ref. 8.

3.1 THIN LENS SPECTROMETER MODEL

This section describes the formalism of the thin lens model for spectrometer systems. The transfer action of each magnet was decomposed into a drift length followed by a lens of power P followed by another drift length. This method resulted in a simple exact optical model for the study of first-order matrix elements and resolutions of the system. It was also used to study the effects of geometric and magnetic parameters on the angular and momentum acceptance of the spectrometers.

In the thin lens equivalence a focusing quadrupole may be replaced by a thin lens of power $P = -K \sin(KL)$, surrounded on each side by a drift space of length $K^{-1} \tan(KL/2)$, where L is the effective length of the quadrupole. The parameter $K = \sqrt{g_0/p_0}$ represents the focusing strength of the field where g_0 is the gradient of the quadrupole and p_0 is the momentum of the particle. A defocusing quadrupole may be replaced by a thin lens of power $P = K \sinh(KL)$, surrounded on each side by a drift space of length $K^{-1} \tanh(KL/2)$. A rectangular dipole magnet with uniform field may be replaced in the momentum dispersive plane by a focusing thin lens of power $P = -\sin \theta/R$, surrounded on each side by a drift space of length $R \tan(\theta/2)$, where R is the radius of curvature of the central trajectory and θ is the deflection angle. A pole face rotation of angle γ acts as a lens of power $P = -\tan \gamma/R$ in the non-bend plane and $P = \tan \gamma/R$ in the bend plane.

The matrix elements that describe the transformation of a particle with initial coordinates (in the horizontal plane) of x_0 and θ_0 passing through a series of N lenses are given by

$$\begin{aligned}
 (x|x_0) &= 1 + \sum_{n=1}^N L_n^h A_n^h \\
 (x|\theta_0) &= \sum_{n=0}^N L_n^h B_n^h \\
 (\theta|x_0) &= \sum_{n=1}^N C_{n-1}^h P_n^h \\
 (\theta|\theta_0) &= 1 + \sum_{n=1}^N D_{n-1}^h P_n^h
 \end{aligned} \tag{3.1}$$

where P_n^h are the powers of each lens, L_0^h is the distance between the origin and the first lens, L_N^h is the distance between the last lens and the detectors, L_1^h through L_{N-1}^h are the distances between the lenses, $A_0^h = 0$, $B_0^h = 1$, $C_0^h = 1$, $D_0^h = L_0^h$ and

$$\begin{aligned}
 A_n^h &= A_{n-1}^h + C_{n-1}^h P_n^h \\
 B_n^h &= B_{n-1}^h + D_{n-1}^h P_n^h \\
 C_n^h &= C_{n-1}^h + L_n^h A_n^h \\
 D_n^h &= D_{n-1}^h + L_n^h B_n^h
 \end{aligned} \tag{3.2}$$

We have used TRANSPORT^[5] notation for the matrix elements and coordinates, as illustrated in Figure 4.

Similar equations can be defined in the vertical plane for particles with initial coordinates y_0 and ϕ_0 . The momentum dispersion matrix elements $(x|\delta_0)$ and $(\theta|\delta_0)$ are calculated from simple matrix algebra using the individual matrix elements of the bending magnets involved. All the necessary formalism to derive the momentum dispersion matrix elements is given in a classical paper by S. Penner.^[9]

Due to the large bend angles of the spectrometers, special care was taken in the evaluation of the effective entrance and exit pole face rotation angles. These angles are different from the geometric ones due to corrections arising from the presence of extended fringing fields and finite horizontal pole widths. The magnitude of these corrections are proportional to the deflection angle in the dipole magnet. The spatial extent of the fringing field causes a reduction of focusing in the non-bend plane and the finite pole width gives rise to change in focusing strength in both planes by curving the iso-induction lines. The measured shapes of the fringing fields of the dipole magnets were used in calculating the corrections^[10,11] to the geometric pole face rotations.

The maximum horizontal acceptance for a given set of i lenses was determined by using equations similar to (3.1) to find the production angles θ_o^i for which rays would just hit apertures of half-width X_i located at the middle of the i^{th} lens, assuming an initial x_o given by the typical beam size. This was done for values of i ranging from 1 to the maximum number of lenses in the system N , plus an additional pass to take into account the width of the detectors. The horizontal acceptance θ was then given by

$$\theta = \min [|\theta_o^1|, |\theta_o^2|, |\theta_o^3|, \dots, |\theta_o^{N+1}|] \quad (3.3)$$

where $\theta_o^i = (X_i - x_o)/G_i^h$ with $G_1^h = L_o^h$ and

$$G_i^h = G_{i-1}^h + L_{i-1}^h \left(1 + \sum_{j=1}^{i-1} G_j^h P_j^h\right) \quad (3.4)$$

for $i > 1$. The maximum vertical acceptance was found in a similar manner. The solid angle $\Delta\Omega$ for the system was then found from the product of the horizontal and vertical acceptances: $\Delta\Omega = \pi\theta\phi$.

The computer program used to implement the above formulas had the ability to fit selected parameters (such as gradients, deflection angles, and drift

distances) to obtain desired matrix elements, minimize the momentum or angular resolutions, and maximize solid angle. Comparisons were made with both TRANSPORT and TURTLE to check that the program was working as expected.

3.2 THE ELECTRON SPECTROMETER

The electron spectrometer is shown in more detail in Figure 2. It was designed to analyze electrons with momenta from 0.25 to 0.64 GeV/c backscattering at 180°. Other design goals were to achieve the largest possible solid angle, moderate momentum and angular resolution, momentum acceptance on the order of $\pm 5\%$, and a large bend angle to place the detectors well out of the path of unwanted background particles.

These goals were met using three powerful 10Q18 quadrupoles for the Q1-Q2-Q3 triplet (see Table 1). They have a large radius and good field uniformity, so that a large solid angle could be obtained without introducing large second-order corrections. The good field uniformity and the large gap of two 29D36 rectangular dipole magnets justified their utilization as B3 and B4. These magnets have 'window-frame' type coils.

In order to maximize the solid angle of the electron spectrometer, the distance from the target center to Q3 was set at the minimum allowed by the mechanical constraints for the installation of the cryogenic target system. Since the momentum was dispersed in the horizontal plane, the focusing action of Q3 was in the vertical plane. This quadrupole provided a large acceptance collection for the vertical angle ϕ_e^o by running close to its maximum strength. The thin lens model was used to optimize this strength, as illustrated in Figure 5. Quadrupole Q2, with opposite polarity, was a limiting aperture for the horizontal angle θ_e^o . The overall solid angle was maximized by making the distance between Q2 and Q3 as short as possible. The field strength of Q1 and the distance from Q1 to Q2 were among the free parameters adjusted to give the desired first-order matrix elements for the system and to obtain the best possible resolutions.

It was desirable to have the B3 bend angle θ_{B3} be as large as possible to preserve the ϕ_o^e acceptance. Although we could have chosen a value for θ_{B3} as large as 25° with no loss in momentum resolution or momentum acceptance, we were forced to choose a value of only 20° to accommodate the angular range of available bellows for the chicane magnets. With the choice $\theta_{B3} = 20^\circ$, the values of θ_{B1} ranged between 4° and 11.5° for the kinematic range of the experiment. The entrance pole face rotation for magnet B3 was fixed at 0° .

The distance between Q1 and B3 was kept as small as possible to preserve solid angle, but was made large enough to allow room for an insertable screen just in front of Q1. This screen was out of the fringe field of B3, and was used to periodically check the alignment of the incident electron beam.

The distance between B3 and B4 was made large enough to allow a straight-ahead beam pipe to be placed between B1 and B3 during set-up and testing of the recoil arm, where B2 was completely removed from the beam line and B1 and B3 were turned off. The bend angle of B4 was made as large as possible to maximize the vertical focusing from the entrance and exit pole face rotations, to obtain moderate momentum resolution, and to move the detectors as far away as possible from the path of background particles. A constraint was that too large a bending angle would cause degradation of resolution due to field non-uniformities and loss of acceptance from geometric limitations. The optimal value for θ_{B4} was found to be 45° .

The final results for the parameters of the beam elements for the electron spectrometer are given in Table 2.

The absence of any first-order momentum dispersion in the vertical direction dictated a parallel-to-point optics for an optimum angular resolution: $(y|y_o) = 0$. All rays with the same ϕ_o^e at the target were brought to a focus at a focal plane located at a distance of 2.683 m from the end of B4. The angular dispersion was -0.08 cm/mr, more than adequate to achieve the desired 8 mr resolution since the wire spacing of the wire chambers in the vertical direction was 0.2 cm.

The optics in the horizontal direction was close to point-to-parallel focusing: $(\theta|\theta_o) \approx 0$. The angle θ^e at the exit of B4 was almost proportional to the relative momentum deviation $\delta_o^e = \Delta p^e/p_o^e$ of the particle and independent of θ_o^e . The momentum resolution was limited by the finite size of the beam spot and by the longitudinal extent of the target, even in the case of a perfect θ^e measurement. The x^e coordinate carried all the θ_o^e information. Point-to-parallel optics was chosen instead of the traditional point-to-point, where $(x|\theta_o) = 0$, for two reasons: it gave a significantly better resolution in the θ_o^e reconstruction and it gave a much bigger momentum acceptance through the vanishing of the $(\theta|\theta_o)$ term.

In this system second-order chromatic and geometric effects were expected to be significant. The first- and second-order matrix elements from the target to the ϕ_o focal plane were calculated using TRANSPORT^[5] and are listed in Table 3. Reverse first- and second-order matrix elements from the detectors back to the target were calculated by generating a set of test rays using the forward matrix elements from TRANSPORT and performing a least-squares fit. The results are listed in Table 4. The electron scattering angles Θ_e were calculated using

$$\pi - \Theta_e = \arctan \left[\sqrt{\tan^2 \theta_o^e + \tan^2 \phi_o^e} \right] \simeq \sqrt{\theta_o^e{}^2 + \phi_o^e{}^2} \quad (3.5)$$

The Monte Carlo program was also run to generate a different set of test rays. It used interpolations of field maps made of magnets B3 and B4 to transport the particles through these magnets, rather than relying on the TRANSPORT matrix elements. The field maps were made using a three-dimensional Hall probe positioned at 2.54 cm intervals in x, y and z at three values of the magnet currents. The absolute calibration of the Hall probe measurements were checked using long coil measurements to measure the integral of the fields as a function of current. The Monte Carlo also took into account measured non-uniformities in the gradient of the quadrupoles. The reverse matrix elements found from a fit to these test rays did not differ significantly from those listed in Table 4, showing that a second-order description of the system was adequate.

The angular and momentum resolutions of the spectrometer were momentum dependent and depended on the beam spot size and the target length. They were further degraded by energy loss and multiple scattering in the targets, vacuum windows, and wire chambers, and the uncertainties in track measurements from the finite wire spacing in the MWPCs. Table 5 gives, for a thin target, the expected resolutions in θ_o^e , ϕ_o^e , and δ_o^e for 0.3 and 0.6 GeV/c scattered electron momenta, calculated using the estimated uncertainties in x^e , y^e , θ^e and ϕ^e at the MWPCs, also given in the Table.

The solid angle $\Delta\Omega_e$ depended strongly upon the target length and was determined by the magnet apertures and the size of the detectors. Figure 6 shows the maximum horizontal and vertical acceptance angles $(\theta_o^e)_{max}$ and $(\phi_o^e)_{max}$ of the electron spectrometer as a function of target position z_o^e . The average solid angles were found to be 22.7, 22.4, 21.5, and 19.4 msr for target lengths of 5, 10, 20, and 40 cm respectively, averaged over a momentum acceptance of $\pm 1\%$. The momentum acceptance was limited by the size of the detectors rather than the magnet apertures. The variation of the solid angle with relative momentum is shown for a thin target in Figure 7.

The optical properties of this spectrometer are illustrated in Figures 8 and 9. In the horizontal plane, rays with same momentum emerged parallel at the exit of the system. In the vertical plane parallel rays from the target ended up at the same spot on the ϕ_o^e focal plane. Figure 8 also illustrates the effect of including second-order matrix elements for typical rays. Second-order effects were much larger for extreme rays, as illustrated in Figure 9.

A configuration using a quadrupole doublet rather than the triplet Q1-Q2-Q3 was also investigated. The triplet solution was chosen because it gave a bigger angular acceptance in the horizontal direction and a larger solid angle for long targets.

3.3 THE BEAM TRANSPORT SYSTEM

Two 18D36 rectangular dipole magnets with very uniform fields were selected for the beam transport system to serve as B1 and B2. Their physical properties are listed in Table 1. The distance L_c between the centers of B1-B2 and B2-B3 is 5.09 m on the beam center-line, the minimum allowed by the B4 location, as shown in Figure 2. A remotely insertable screen was installed before the entrance of magnet B1 for periodic alignment of the electron beam entering the transport system. Two 'roller screens' located upstream of B1 are part of the permanent ESA facilities and were also used for beam alignment. All screens were removed for normal data taking.

The magnet B2 was mounted on a carriage that moved on rails and was positioned remotely from the experimental control area. Constraints from the flexibility of bellows in the movable vacuum system between B1 and B3 limited the θ_{B1} angular range to be 4° to 11.5° .

The target center was located 24.8 m downstream of the End Station A target pivot. The symmetric arrangement and operation of the chicane magnets B1, B2 and B3 preserved the initial achromaticity of the electron beam; its final position and divergence after B3 were independent of the momentum spread. The matrix elements $(x|\delta_0)$ and $(\theta|\delta_0)$ of the total transformation from the beginning of the switchyard to the target were identically zero.

The A-Line^[12] quadrupoles in the beam switchyard were used for imaging the beam from the end of the accelerator to the new target position. The TRANSPORT model^[13] for the A-line was used to obtain quadrupole gradients that both optimized beam transmission through the narrow apertures of the switchyard and gave horizontal and vertical magnifications of nearly 1 : 1 at the target when Q1, Q2, and Q3 were turned off. The effect of the quadrupole triplet Q1-Q2-Q3 varied with kinematics, resulting in a typical beam spot size of a few mm and a typical divergence of 1 mr at the target. These spatial and angular spreads were

well within the resolution tolerances for the experiment, being much smaller than the spreads caused by multiple scattering in the targets.

3.4 THE RECOIL SPECTROMETER

The recoil spectrometer is shown in Figure 3. The quadrupole triplet Q4-Q5-Q6 was carefully chosen and tuned to ensure a good overlap of the acceptances of the two arms for a range of target lengths. The long targets and the relatively high momentum of the recoiling deuterons made that task difficult.

Extensive calculations with a thin lens acceptance model for the recoil spectrometer, similar to that used for the electron spectrometer, resulted in the selection of an 8Q32 quadrupole for Q4 and a 10Q36 quadrupole for Q5. Both have high gradients similar to the quadrupoles used in the electron spectrometer, but are essentially twice as long, allowing much higher momentum particles to be focused (see Table 1). As in the electron spectrometer, Q4 is focusing in the vertical direction and Q5 in the horizontal. The field strengths of Q4 and Q5, the drift distance between them, and the drift length from the target to Q4 were the crucial parameters in achieving the desired solid angle for this spectrometer.

A third quadrupole was found to be necessary on this side for the transmission of the recoil particles through the long path and narrow apertures of the bending magnets of the recoil system. The length and strength of Q6 and its distance from Q5 were free parameters in the spectrometer optimization. Although a 10Q36 quadrupole would have provided better focusing, a shortage of power supplies dictated the use of a 10Q18 quadrupole as Q6. The current required for this quadrupole was slightly less than that of Q5, permitting the two quads to be run in series from a single power supply. A small current bypass of variable impedance was coupled in parallel to Q6 to fine tune the current flowing in that quadrupole.

The split magnet B5 had to be wide enough to both bend the deuterons by a reasonably large angle (to minimize the distance to B6) and at the same

time transmit the electron beam onto the dump. The separation between B5 and B6 was determined by the need to accommodate a 90 cm diameter beam pipe behind B5 to transmit the photons produced in the target to a shielded downstream photon beam dump. The only magnet available that could both bend the deuterons by a large angle and simultaneously bend the electrons to the dump without having them hit the magnet iron was a 26D72 rectangular dipole magnet with a total horizontal aperture of 100 cm (see Table 1). This large width permitted a bend angle θ_{B5} for the recoil nuclei of 15° , but resulted in relatively poor field uniformity. For this reason we made extensive field measurements of this magnet, similar to the ones made of B3 and B4. The separation between B5 and Q6 was chosen to provide enough space for another beam viewing screen.

The anticipation of large background rates in the deuteron detectors determined the need for the three bending magnets B6-B7-B8. This background was expected to be low energy, multi-bounce charged particles or photons originating mainly from the region of the split magnet B5. These magnets give many kG-m of sweeping power for charged background particles and put B5 out of line-of-sight of the detectors to protect them from direct photons. Originally the recoil spectrometer was designed and built without magnet B8. A background test-run showed that this magnet was necessary to keep the counting rates in the recoil detectors at tolerable levels.

Three 18D72 rectangular bending magnets with window-frame type coils were utilized for B6, B7 and B8. They were the most powerful, high quality, long magnets available. The separation between them was kept at the minimum required for mechanical installation. All three magnets were run in series from one power supply. The bend angles were 17° for B6 and B7, and 16.45° for B8. This choice of bending angles put the detectors far away from the straight-ahead-beam line without running the magnets in the saturation region.

The beam elements of the recoil spectrometer are listed in Table 6 for the maximum 2.603 GeV/c tune. The first- and second-order forward transport

coefficients, from the target center to the center of the recoil side wire chambers, are given in Table 7. The optics in the horizontal direction was close to point-to-parallel. In the vertical plane it was found impossible to achieve parallel-to-point optics and at the same time to match the solid angles of the two arms, so a compromise optics solution was chosen. The optical properties of this spectrometer are pictured in Figures 10 and 11. These figures show some extreme rays originating from the target, plotted as a function of longitudinal position through the spectrometer up to the center of the wire chambers. The reverse first- and second-order matrix elements are tabulated in Table 8. They were obtained in a method similar to that used for the reverse matrix coefficients of the electron spectrometer.

In order to facilitate the calculation of the double-arm acceptance, a design requirement was that the solid angle of the recoil spectrometer subtend that of the electron spectrometer for elastic scattering kinematics. In terms of the maximum acceptance angles of the electron spectrometer, the angles required for the recoil spectrometer were given by:

$$(\phi_o^r)_{max} = \arcsin \left[\frac{p'_e}{p_r} \sin (\phi_o^e)_{max} \right] \quad (3.6)$$

$$(\theta_o^r)_{max} = \arcsin \left[\frac{p'_e}{p_r} \sin (\theta_o^e)_{max} \right] \quad (3.7)$$

where p_r is the momentum of the recoil nuclei. The magnitudes of $(\phi_o^r)_{max}$ and $(\theta_o^r)_{max}$ were further increased to take into account multiple scattering of the recoil particles in the targets. Figure 12 shows the maximum acceptance angles of the recoil spectrometer (solid lines) as well as the design requirements (dashed curves). It can be seen the recoil acceptance angles were everywhere larger than that required to subtend those of the electron spectrometer for elastic kinematics.

The recoil momentum acceptance was limited by the apertures of the bending magnets. It was small compared to the momentum acceptance of the electron

spectrometer because of the large momentum dispersion of the dipole magnets B5-B6-B7-B8, but sufficient to cover the momentum spread of the deuterons from elastic kinematics and from energy loss in the targets. The variation of the recoil spectrometer solid angle with relative momentum is shown for a thin target in Figure 13.

The angular and momentum resolutions were determined by the optics of the recoil spectrometer, energy loss and multiple scattering in the target, vacuum windows, and detectors, and by the finite spatial resolution of the MWPCs. When the spectrometer was designed it was not considered important to have good angular and momentum resolution because elastic events were to be simply identified from electron-deuteron time-of-flight measurements. Subsequently it was found that measurements of the deuteron momentum were needed to eliminate an unanticipated source of background.^[1] Table 9 shows typical values for resolutions in the reconstructed kinematic quantities for a thin target calculated using the estimated uncertainties in track position and angles measured at the MWPCs.

3.5 THE BEAM DUMP

The beam dump was a water-cooled copper block contained in a stainless steel jacket approximately 56 cm high, 18 cm wide, and 70 cm long. Except for the side facing the beam, it was surrounded by a layer of lead approximately 20 cm thick. A 60 cm diameter toroid charge monitor was mounted in front on the dump to measure the transmission of the beam through the spectrometer system. High intensity beam could only be delivered into the End Station when the transmission was above a predetermined threshold.

Magnet B5 deflected the electron beam towards the dump by an angle θ_d given by

$$\theta_d = \arcsin \left(\frac{p_r}{p_e} \sin \theta_{B5} \right) \quad (3.8)$$

Its value ranged from 19° to 25° for electron-deuteron elastic scattering from $Q^2 = 1$ to 5 $(\text{GeV}/c)^2$ and electron-proton elastic scattering from $Q^2 = 0.25$ to 1.25 $(\text{GeV}/c)^2$. The beam dump, lead shielding, and toroid monitor were mounted on a remotely controlled platform that could be moved to accommodate this range of deflection angles. A ZnS screen viewed by a TV camera was mounted on the front face of the dump. It was used to verify the alignment of the dump for each new recoil spectrometer setting and each new beam energy.

The dump location was chosen as a compromise between the desire to have it close to the exit of B5, where the beam spot was smaller, and the need for adequate shielding. For radiation protection it was necessary to surround the dump area with 1.5 m of iron and 2 m of concrete. The straight-ahead vacuum pipe from B5 to the photon dump needed to be large enough to prevent the intense photon beam produced in the target from striking the vacuum chamber and producing background particles near the exit of B5. These requirements forced the dump to be located 7.5 m from B5.

The beam spot size on the dump was estimated using the DECAY TURTLE program, taking into account the energy spread from ionization losses and the angular spread from multiple scattering in the targets. Figure 14 shows the beam spatial distributions on the dump for the two limiting cases of electron-deuteron elastic scattering: $Q^2 = 1$ and 5 $(\text{GeV}/c)^2$, with 10 cm and 40 cm long deuterium targets respectively. The shape of the beam envelope on the dump changed with kinematics since the ratios of the gradients of the quadrupoles Q4-Q5-Q6 to the beam momentum varied with the recoil particle momentum.

4. CALIBRATION

The momentum calibration of the electron spectrometer was performed using electron-proton elastic scattering. At several known scattered electron momenta, the fields of the bending magnets B3 and B4 were adjusted to center the electron elastic peak distributions in x^e and θ^e measured at the center of the wire chambers. The initial settings were calculated using effective magnet lengths and assuming sharp cutoff fringing fields for B3 and B4 without taking into account the displacement of the central ray due to the extent of the fringing field as discussed by Enge.^[10,11] When this displacement was taken into account, the calculated current settings of the two magnets agreed with those required to center the elastic peak distributions measured at the center of the wire chambers, as shown in Figure 15.

The momentum dispersion matrix elements $(x|\delta_o)$ and $(\theta|\delta_o)$ were extracted by sweeping the electron-proton elastic peak distributions across the acceptance of the spectrometer in special calibration runs using the hydrogen target. This was done by lowering and raising the central momentum of the spectrometer while keeping the beam energy fixed. The values of $(x|\delta_o)$ and $(\theta|\delta_o)$ measured at the center of the wire chambers were found to be in excellent agreement with the predictions.

The angular dispersion in the vertical direction was verified in a special calibration measurement by placing a tungsten shield between a thin Al target and Q3. The shield was pierced by holes placed along the vertical axis. In this way, electrons with well-defined vertical angles ϕ_o^e were imaged at specific y^e locations in the wire chambers as shown in Figure 16. Figure 17 shows the data for the y^e measurement at the center of the MWPC and the prediction of the optics model of the spectrometer. The measurements were found to be in good agreement with the model.

The recoil spectrometer was calibrated in the momentum range of 1.5 to 2.5 GeV/c with an electron beam and in the range 0.7 to 1.5 GeV/c with double-arm

ep elastic scattering. For the high momentum calibration, the field direction of bending magnets B5-B6-B7-B8 was reversed and a low intensity electron beam was run through the spectrometer. The fields of these magnets were adjusted to center the beam on two fluorescent screens placed 3.8 m apart on the spectrometer axis after B8. The momentum dispersion matrix elements and momentum acceptance were also measured in the course of this procedure. For momenta below 1.5 GeV/c, the magnet currents were adjusted to center elastic recoil proton peak distributions in a manner similar to that used to calibrate the electron spectrometer. The measured dispersions agreed very well with the optics calculations, and the calibration data from the two momentum ranges joined smoothly.

5. PERFORMANCE

The performance of the system was evaluated using *ep* elastic scattering, for which the cross sections are well-known. Both single-arm (electron spectrometer only) and double-arm (both spectrometers) cross sections were measured for a variety of target lengths. Effective solid angles (the convolution of geometric solid angles with radiative and ionization energy losses, multiple scattering, etc.) were calculated with the Monte Carlo program.^[7] The program was also used to generate momentum and angle spectra which could be compared to the measured distributions.

The Monte Carlo program was needed in the evaluation of the performance so that the effects of energy loss, multiple scattering, nuclear absorption, apertures, finite target length, and elastic kinematics could all be taken into account simultaneously. It could also take into account the detailed field maps that were made of magnets B3, B4, and B5, as well as the measured non-uniformity in the gradients of the quadrupoles. Electron events were generated by randomly choosing initial values for $z_o^e = -z_o^r$ within the given target length and for θ_o^e and ϕ_o^e within ranges larger than the spectrometer acceptance. Values for x_o^e and y_o^e were chosen within the given beam spot size. A value for E was chosen within

the assumed energy defining slits using a Gaussian distribution. The value of E was corrected for ionization energy loss using Landau distributed values around the most probable energy loss, which was evaluated with the density effect properly taken into account.^[14] It was also corrected for radiative energy loss using the formula of G. Miller^[15] to approximate the radiation probability distribution given by Mo and Tsai.^[16] The variation of the cross section with Q^2 was taken into account in the selection of initial events. The angle of the incident electron was corrected for multiple scattering and the values of p'_e , p_r , θ'_o , and ϕ'_o were then calculated using elastic kinematics. The final electron momentum was corrected for ionization and radiative energy loss, while the recoil particle energy was corrected for ionization energy loss only. Multiple scattering was taken into account for both particles. The nuclear absorption probability for the recoil particle was evaluated. Particles were made to pass through the spectrometers by stepping through the measured magnetic fields and checking to see if they hit any apertures. Field maps were not made of magnets B6-B8, so first-order TRANSPORT coefficients were used in this case. Spectra were made of events which successfully made it to the detectors. Effective single-arm and double-arm solid angles were calculated using the ratio of successful events to the number of trials.

The agreement between observed elastic ep scattering and that predicted by the Monte Carlo was in general good. Figures 18 through 21 show the comparison between data and Monte Carlo predictions for the most important distributions at the detectors for ep elastic scattering from a 10 cm hydrogen target at 0.937 GeV incident beam energy. It can be seen that very good agreement is found on the electron side, while on the recoil side the measured elastic peaks are slightly broader than those predicted by the model. Agreement with distributions not shown (i.e. x^e , ϕ^e , y^r and ϕ^r) were generally good.

The Monte Carlo program was used to calculate the effective single- and double-arm solid angles for each of the ep data runs. The results were found to vary slowly with beam energy for a given target length, and are shown as a

function of target length for a beam energy of 1.0 GeV in Figure 22. Also shown are the geometric solid angles. The principal reason that the effective solid angles were smaller than the geometric ones was the loss of electrons and recoil particles due to radiative energy loss by the incident and scattered electrons.

The calculated solid angles were used to evaluate the double-arm absolute cross sections for all of the ep elastic measurements. The results are compared to previous data^[17] in Figure 23, where it can be seen that the agreement is quite good. Cross sections were measured at each beam energy using several of the four target lengths available. No dependence on target length was observed at any of the beam energies; the results shown in Figure 23 are for the average over all targets used. The good agreement between different target lengths shows that the Monte Carlo program correctly predicts the differences in effective solid angles due to radiative effects, energy loss, multiple scattering, and absorption.

As a further check, cross sections were calculated using only the electron arm data, not requiring a coincidence with the recoil proton. In this case, a subtraction was made for electrons back-scattering from the aluminium endcaps of the targets. The ratios of single-arm to double-arm cross sections (averaged over target length) are shown in Figure 24. The ratios are all close to 1, showing that the Monte Carlo program correctly predicts the loss of protons due to radiative corrections, multiple scattering, momentum acceptance, nuclear absorption, and apertures.

6. SUMMARY

A double-arm 180° spectrometer system for electron scattering from deuterium has been described. Lumped quadrupole elements on the beam line provided a large acceptance collection for the back-scattered electrons and the recoil nuclei while having little effect on the incident electron beam. The large solid angle of this system made possible elastic and inelastic cross section measurements from deuterium at high momentum transfers. It was the first facility for 180° electron scattering in which recoiling nuclei were detected in coincidence at 0°. The analysis results found the performance of the system in very good agreement with the design specifications and with the predictions of the second-order models. With minor modifications, the system could be used for elastic and inelastic electron scattering from Tritium.

We acknowledge the work of Z. Vassilian in designing and supervising the modifications to the magnets and of D. R. Jensen in performing the magnetic measurements of all the quadrupoles. J. Lambert, A. Lung, and G. Peterson helped in measuring the field maps of the dipole magnets. C. Hudspeth was of great help in the assembly of the spectrometers. The support of M. M. Berndt, J. F. Brown, H. Harvey, L. Otts and the rest of the SLAC staff is greatly appreciated. This work was supported by the Department of Energy Contract DOE-AC03-76SF00515 and National Science Foundation Grant PHY85-10549.

REFERENCES

1. R. G. Arnold *et al.*, Phys. Rev. Lett. **58**, 1723 (1987).
2. R. F. Koontz *et al.*, "Commissioning and Operation of the Nuclear Physics Injector at SLAC", SLAC-PUB-3615, 1985, published in Particle Accelerator Conference, Vancouver, Canada, 1985.
3. G.A. Peterson *et al.*, Nucl. Instr. and Meth. **160**, 375 (1979).
4. G. J. C. van Niftrik *et al.*, Nucl. Instr. and Meth. **93**, 301 (1971).
5. K. L. Brown *et al.*, "TRANSPORT A Computer Program for Designing Charged Particle Beam Transport Systems", SLAC Report No. 91, 1977.
6. D. C. Carey *et al.*, "DECAY TURTLE, A Computer Program for Simulating Charged Particle Beam Transport Systems, Including Decay Calculations", SLAC Report No. 246, 1982.
7. A. T. Katramatou, "DEMON - A Monte Carlo Program for Electron-Deuteron Scattering in Coincidence at 180 Degrees", SLAC Report No. NPAS-TN-86-8.
8. G. G. Petratos, "Design and Operation of a Double Arm 180° Spectrometer System for Magnetic Electron Scattering from Deuterium", SLAC Report No. NPAS-TN-86-7.
9. S. Penner, Rev. Sci. Instr. **32**, 150 (1961).
10. H. A. Enge, Rev. Sci. Instr. **35**, 278 (1964).
11. H. A. Enge, "Deflecting Magnets", in Focusing of Charged Particles, edited by A. Septier (New York, Academic Press, 1967), Vol. 2.
12. H. Weidner *et al.*, "Design, Construction, and Early Operating Experience of the SLAC Beam Switchyard and Experimental Areas", SLAC-PUB-285, 1967, published in IEEE Transactions on Nuclear Science, Vol. NS-14, No. 3, 918 (1967).

13. H. S. Butler *et al.*, "Specifications for the Beam Transport Systems to End Stations A and B", SLAC Report No. 29, 1964.
14. T. Tabata and R. Ito, Nucl. Instr. Meth., **158**, 521 (1979); R. M. Sternheimer, R. F. Peirls, Phys. Rev. **B3**, 3681 (1971).; R. M. Sternheimer *et al.*, "The Density Effect for Ionization Loss of Charged Particles in Various Substances", BNL-31435, 1982.
15. G. Miller, "Inelastic Electron Scattering at Large Angles", Ph.D Thesis, SLAC-Report 129, (1971).
16. L. W. Mo, Y. S. Tsai, Rev. Mod. Phys. **41**, 205, (1969); Y. S. Tsai, "Radiative Corrections to Electron Scatterings", SLAC-PUB-848, 1971.
17. L. E. Price *et al.*, Phys. Rev. **D4**, 45 (1971).

TABLE CAPTIONS

1. Physical properties of the magnets used in the system.
2. The beam elements of the electron spectrometer for the maximum 0.635 GeV/c tune. The values of L_{eff} are the effective lengths of the central trajectory. The first drift length is from the target center. The last drift length is to the ϕ_0 focal plane. The center of the MWPCs is 0.325 m upstream of the ϕ_0^e focal plane. The parameters α^h and α^v are the effective entrance pole face rotation angles in the horizontal and vertical direction. The parameters β^h and β^v are the effective exit pole face rotation angles in the horizontal and vertical direction.
3. The first- and second-order forward matrix elements of the electron spectrometer from the target center to the ϕ_0 focal plane, determined from TRANSPORT. The units of x_0 and y_0 are cm and the units of θ_0 and ϕ_0 are mr. The momentum deviation from the central trajectory δ_0 is in percent.
4. The first- and second-order reverse matrix elements of the electron spectrometer from the ϕ_0 focal plane to the target center. The units of x and y are cm and the units of θ and ϕ are mr.
5. Resolutions in reconstructed quantities and in positions and angles measured at the MWPCs for a thin target at two values of the scattered electron momentum.
6. The beam elements of the recoil spectrometer for the maximum 2.603 GeV/c tune. The values of L_{eff} are the effective lengths of the central trajectory. The first drift is from the target center. The last drift is to the center of the MWPCs. The parameters α^h and α^v are the effective entrance pole face rotation angles in the horizontal and vertical direction. The parameters β^h and β^v are the effective exit pole face rotation angles in the horizontal and vertical direction.

7. The first- and second-order forward matrix elements of the recoil spectrometer from the target center to the center of the wire chambers, determined from TRANSPORT. The units of x_0 and y_0 are cm and the units of θ_0 and ϕ_0 are mr. The momentum deviation δ_0 from the central trajectory is in percent.
8. The first- and second-order reverse matrix coefficients of the recoil spectrometer from the center of the wire chambers to the target. The units of x and y are cm and the units of θ and ϕ are mr.
9. Resolutions in reconstructed quantities and in positions and angles measured at the MWPCs for a thin target at two values of the recoil particle momentum.

TABLE 1

Dipole Magnets				
Name	Length	Width	Gap	Max. Field
B1, B2	91.4 cm	45.7 cm	15.2 cm	18 kG
B3	91.4 cm	73.7 cm	25.6 cm	18 kG
B4	91.4 cm	73.7 cm	28.0 cm	16 kG
B5	182.9 cm	100 cm	20.0 cm	13 kG
B6, B7, B8	182.9 cm	46.2 cm	25.4 cm	15 kG

Quadrupoles			
Name	Length	Radius	Max. Field
Q1, Q2, Q3, Q6	45.7 cm	12.86 cm	12 kG
Q4	81.3 cm	10.47 cm	15 kG
Q5	91.4 cm	12.86 cm	13 kG

TABLE 2

Beam element	Action	L_{eff} (m)	Strength (kG or kG/m)
Drift		0.600	
Quadrupole Q3	Vertical focus	0.490	90.19
Drift		0.354	
Quadrupole Q2	Vertical defocus	0.490	69.83
Drift		0.354	
Quadrupole Q1	Vertical focus	0.490	38.28
Drift		1.204	
Pole Rotation	$\alpha^h = 0.0^\circ \alpha^v = 0.0^\circ$		
Dipole B3	20.01° horizontal bend	1.209	6.117
Pole Rotation	$\beta^h = 18.81^\circ \beta^v = 16.93^\circ$		
Drift		2.145	
Pole Rotation	$\alpha^h = 20.12^\circ \alpha^v = 15.50^\circ$		
Dipole B4	45.33° horizontal bend	1.237	13.548
Pole Rotation	$\beta^h = 20.12^\circ \beta^v = 15.50^\circ$		
Drift		2.683	

TABLE 3

	x (cm)	θ (mr)	y (cm)	ϕ (mr)
x_o	-2.61	-4.31	0.0	0.0
θ_o	0.18	-0.08	0.0	0.0
y_o	0.0	0.0	0.0	12.01
ϕ_o	0.0	0.0	-8.3×10^{-2}	4.9×10^{-3}
δ_o	-4.79	-11.06	0.0	0.0
x_o^2	2.2×10^{-3}	1.4×10^{-2}	0.0	0.0
$x_o\theta_o$	9.0×10^{-4}	-5.6×10^{-4}	0.0	0.0
$x_o y_o$	0.0	0.0	2.7×10^{-2}	1.8×10^{-2}
$x_o \phi_o$	0.0	0.0	1.2×10^{-4}	2.8×10^{-4}
$x_o \delta_o$	0.31	0.30	0.0	0.0
θ_o^2	8.1×10^{-7}	7.5×10^{-6}	0.0	0.0
$\theta_o y_o$	0.0	0.0	-3.0×10^{-3}	-7.3×10^{-3}
$\theta_o \phi_o$	0.0	0.0	-4.9×10^{-5}	-3.1×10^{-4}
$\theta_o \delta_o$	3.7×10^{-2}	3.1×10^{-2}	0.0	0.0
y_o^2	5.6×10^{-3}	7.8×10^{-2}	0.0	0.0
$y_o \phi_o$	5.4×10^{-4}	1.3×10^{-3}	0.0	0.0
$y_o \delta_o$	0.0	0.0	-0.13	-0.30
ϕ_o^2	2.2×10^{-5}	3.3×10^{-5}	0.0	0.0
$\phi_o \delta_o$	0.0	0.0	-2.0×10^{-3}	-1.9×10^{-2}
δ_o^2	4.6×10^{-2}	0.13	0.0	0.0

TABLE 4

	x_o (cm)	θ_o (mr)	y_o (cm)	ϕ_o (mr)	δ_o (%)
x	-6.1×10^{-3}	4.79	-1.2×10^{-5}	1.6×10^{-3}	-3.6×10^{-2}
θ	1.0×10^{-3}	-2.06	-3.7×10^{-6}	1.6×10^{-4}	-7.5×10^{-2}
y	2.2×10^{-4}	2.9×10^{-3}	-6.0×10^{-3}	-12.00	-1.3×10^{-4}
ϕ	1.2×10^{-4}	-1.3×10^{-2}	8.2×10^{-2}	-4.4×10^{-3}	3.1×10^{-4}
x^2	-2.1×10^{-4}	9.9×10^{-3}	1.3×10^{-5}	-4.4×10^{-4}	-2.1×10^{-4}
$x\theta$	-5.6×10^{-6}	3.6×10^{-2}	-6.5×10^{-6}	3.7×10^{-4}	-1.2×10^{-3}
xy	-3.6×10^{-4}	-3.9×10^{-4}	-9.3×10^{-4}	2.7×10^{-2}	1.2×10^{-4}
$x\phi$	-2.6×10^{-4}	3.8×10^{-4}	7.0×10^{-5}	-6.9×10^{-3}	6.3×10^{-5}
θ^2	4.4×10^{-5}	-1.7×10^{-2}	-6.5×10^{-7}	-6.3×10^{-5}	6.5×10^{-4}
θy	2.0×10^{-4}	4.5×10^{-5}	2.1×10^{-3}	-3.8×10^{-2}	-6.5×10^{-5}
$\theta\phi$	8.4×10^{-5}	3.9×10^{-5}	-1.8×10^{-4}	1.2×10^{-2}	-2.2×10^{-5}
y^2	3.3×10^{-4}	-1.4×10^{-3}	4.8×10^{-7}	-3.5×10^{-4}	2.8×10^{-4}
$y\phi$	-5.5×10^{-4}	1.9×10^{-3}	-3.8×10^{-5}	5.7×10^{-4}	2.5×10^{-5}
ϕ^2	-2.2×10^{-4}	1.7×10^{-3}	1.7×10^{-5}	1.2×10^{-4}	4.9×10^{-5}

TABLE 5

$$p'_e = 0.3 \text{ GeV/c} \quad p'_e = 0.6 \text{ GeV/c}$$

Resolutions in reconstructed quantities

$\Delta\theta_0$ (mr)	± 8.6	± 5.8
$\Delta\phi_0$ (mr)	± 5.6	± 3.2
$\Delta\delta_0$ (%)	± 0.60	± 0.32

Resolutions at MWPCs

Δx (cm)	± 0.4	± 0.2
$\Delta\theta$ (mr)	± 5.3	± 2.8
Δy (cm)	± 0.4	± 0.2
$\Delta\phi$ (mr)	± 5.0	± 2.3

TABLE 6

Beam element	Action	L_{eff} (m)	Strength (kG or kG/m)
Drift		0.881	
Quadrupole Q4	Vertical focus	0.905	122.25
Drift		0.341	
Quadrupole Q5	Vertical defocus	0.959	96.81
Drift		0.354	
Quadrupole Q6	Vertical focus	0.490	91.37
Drift		0.740	
Pole Rotation	$\alpha^h = 0.00^\circ \alpha^v = 0.00^\circ$		
Dipole B5	15.00° horizontal bend	2.061	11.027
Pole Rotation	$\beta^h = 14.75^\circ \beta^v = 14.21^\circ$		
Drift		4.879	
Pole Rotation	$\alpha^h = 7.75^\circ \alpha^v = 6.99^\circ$		
Dipole B6	17.00° horizontal bend	2.099	12.275
Pole Rotation	$\beta^h = 7.75^\circ \beta^v = 6.99^\circ$		
Drift		0.965	
Pole Rotation	$\alpha^h = 7.75^\circ \alpha^v = 6.99^\circ$		
Dipole B7	17.00° horizontal bend	2.099	12.275
Pole Rotation	$\beta^h = 7.75^\circ \beta^v = 6.99^\circ$		
Drift		0.960	
Pole Rotation	$\alpha^h = 7.51^\circ \alpha^v = 6.78^\circ$		
Dipole B8	16.45° horizontal bend	2.098	11.881
Pole Rotation	$\beta^h = 7.51^\circ \beta^v = 6.78^\circ$		
Drift		3.869	

TABLE 7

	<i>x</i> (cm)	<i>θ</i> (mr)	<i>y</i> (cm)	<i>ϕ</i> (mr)
x_o	-2.92	-2.22	0.0	0.0
$θ_o$	0.58	0.10	0.0	0.0
y_o	0.0	0.0	-5.64	2.26
$ϕ_o$	0.0	0.0	-0.14	-0.12
$δ_o$	11.56	11.11	0.0	0.0
x_o^2	-1.6×10^{-3}	-3.0×10^{-3}	0.0	0.0
$x_oθ_o$	-8.6×10^{-4}	4.2×10^{-4}	0.0	0.0
$x_o y_o$	0.0	0.0	-3.9×10^{-3}	8.6×10^{-3}
$x_o ϕ_o$	0.0	0.0	3.0×10^{-4}	1.8×10^{-4}
$x_o δ_o$	0.35	0.18	0.0	0.0
$θ_o^2$	5.4×10^{-5}	-1.5×10^{-5}	0.0	0.0
$θ_o y_o$	0.0	0.0	4.3×10^{-4}	1.1×10^{-3}
$θ_o ϕ_o$	0.0	0.0	-5.7×10^{-5}	4.0×10^{-5}
$θ_o δ_o$	6.7×10^{-2}	2.8×10^{-2}	0.0	0.0
y_o^2	-1.7×10^{-2}	-6.6×10^{-3}	0.0	0.0
$y_o ϕ_o$	-1.1×10^{-3}	-2.6×10^{-4}	0.0	0.0
$y_o δ_o$	0.0	0.0	-0.11	-0.17
$ϕ_o^2$	-1.5×10^{-5}	-1.3×10^{-5}	0.0	0.0
$ϕ_o δ_o$	0.0	0.0	8.5×10^{-3}	-5.2×10^{-3}
$δ_o^2$	-0.10	-0.13	0.0	0.0

TABLE 8

	x_o (cm)	θ_o (mr)	y_o (cm)	ϕ_o (mr)	δ_o (%)
x	-4.1×10^{-3}	2.10	3.4×10^{-6}	1.6×10^{-4}	-1.9×10^{-2}
θ	-1.2×10^{-3}	-2.19	-4.4×10^{-6}	-3.0×10^{-4}	0.11
y	1.8×10^{-4}	1.9×10^{-3}	-0.12	-2.25	6.7×10^{-5}
ϕ	-4.7×10^{-4}	-1.5×10^{-3}	0.14	-5.63	-1.1×10^{-4}
x^2	4.8×10^{-4}	3.3×10^{-3}	-2.9×10^{-6}	-1.5×10^{-4}	1.7×10^{-4}
$x\theta$	-9.4×10^{-4}	-2.1×10^{-2}	1.0×10^{-5}	3.3×10^{-4}	-7.3×10^{-4}
xy	-1.8×10^{-6}	1.8×10^{-4}	1.9×10^{-4}	-5.5×10^{-3}	4.7×10^{-6}
$x\phi$	-4.2×10^{-4}	-2.5×10^{-4}	3.0×10^{-4}	3.1×10^{-3}	-7.4×10^{-5}
θ^2	4.6×10^{-4}	1.9×10^{-2}	-5.4×10^{-6}	-1.7×10^{-4}	6.9×10^{-4}
θy	-3.2×10^{-4}	-5.0×10^{-4}	-6.6×10^{-4}	2.1×10^{-2}	-6.4×10^{-5}
$\theta\phi$	6.7×10^{-4}	7.5×10^{-4}	-1.1×10^{-3}	-1.3×10^{-2}	1.3×10^{-4}
y^2	-1.1×10^{-3}	-1.5×10^{-3}	-1.8×10^{-5}	2.5×10^{-4}	-2.1×10^{-4}
$y\phi$	2.9×10^{-3}	5.1×10^{-3}	3.1×10^{-5}	-3.3×10^{-4}	6.0×10^{-4}
$-\phi^2$	-1.2×10^{-3}	-3.5×10^{-3}	-9.0×10^{-6}	4.6×10^{-6}	-2.1×10^{-4}

TABLE 9

$p_r = 1.0 \text{ GeV/c}$ $p_r = 2.6 \text{ GeV/c}$

Resolutions in reconstructed quantities

$\Delta\theta_o$ (mr)	± 8.3	± 4.0
$\Delta\phi_o$ (mr)	± 17.4	± 5.6
$\Delta\delta_o$ (%)	± 0.41	± 0.23

Resolutions at MWPCs

Δx (cm)	± 0.8	± 0.2
$\Delta\theta$ (mr)	± 3.2	± 1.4
Δy (cm)	± 0.8	± 0.2
$\Delta\phi$ (mr)	± 3.1	± 1.0

FIGURE CAPTIONS

1. The 180° double-arm spectrometer system, placed between the SLAC 8 GeV/c and 20 GeV/c spectrometers. The elements B1 to B8 are dipole magnets and Q1 to Q6 are quadrupoles. Shown also are the detector systems, the target chamber, the beam dump, and the concrete and iron shielding.
2. The electron spectrometer and the incident beam transport system. Shown also are the vacuum chambers, the target scattering chamber, the electron detector system, and the B1 and B3 screens. The deflection angles θ_{B1} through θ_{B4} and X_c , the lateral displacement of B2, are discussed in the text.
3. The recoil spectrometer and the beam dump. Also shown are the vacuum system, the target scattering chamber, the recoil detection system, the dump toroid and the B5 and dump screens.
4. The coordinate systems (x^e, y^e, z^e) and (x^r, y^r, z^r) of the electron and recoil spectrometers. The origin of both systems is the target center. Shown are the initial horizontal angles θ_o^e and θ_o^r and initial vertical angles ϕ_o^e and ϕ_o^r for a typical electron and recoil particle. The total scattering angles Θ_e and Θ_r are also shown.
5. The maximum acceptance angles $(\theta_o^e)_{max}$ and $(\phi_o^e)_{max}$ of the electron spectrometer for rays originating at the center of the target versus the pole-tip field of quadrupole Q3. The curves were calculated using the thin lens model described in the text. For a given value of B_{Q3} , the focusing strengths of Q1 and Q2 were adjusted to obtain parallel-to-point optics in the vertical direction and point-to-parallel optics in the horizontal direction. The arrow indicates the value chosen for B_{Q3} to maximize the spectrometer acceptance.
6. The maximum acceptance angles $(\theta_o^e)_{max}$ and $(\phi_o^e)_{max}$ of the electron spectrometer for rays originating along the beam axis as a function of position

z_o^e near the target center. The results were computed using the thin lens model after the magnet positions and field strengths were fixed to maximize the acceptance at $z_o^e = 0$.

7. The solid angle of the electron spectrometer as a function of relative momentum δ_o^e for a thin target as calculated from the Monte Carlo model.
8. The optical properties of the electron spectrometer for some typical rays:
a) the point-to-parallel focusing in the horizontal plane; two rays are shown with different θ_o^e , each with $y_o^e = \phi_o^e = x_o^e = 0$ and $\delta_o^e = -1\%$. b) the parallel-to-point focusing in the vertical plane; two rays are shown with different y_o^e , each with $x_o^e = \theta_o^e = \delta_o^e = 0$ and $\phi_o^e = 80$ mr. The rays were traced using the TRANSPORT model. The dashed curves (indistinguishable from the solid lines in plot b) were obtained using only first-order matrix elements, while for the solid curves both first- and second-order matrix elements were used. The horizontal solid lines indicate, from left to right, the apertures in magnets Q3, Q2, Q1, B3 and B4.
9. Optical properties of the electron spectrometer for two extreme rays showing the large chromatic second-order effects: a) horizontal plane with $y_o^e = \phi_o^e = 0$ and large values for x_o^e , θ_o^e and δ_o^e and b) vertical plane with $x_o^e = \theta_o^e = 0$ and large values for y_o^e , ϕ_o^e and δ_o^e . The rays were traced using the TRANSPORT model. The solid curves were obtained using both first- and second-order matrix elements, while for the dashed curves only first-order matrix elements were used. The horizontal solid lines indicate, from left to right, the apertures in magnets Q3, Q2, Q1, B3 and B4.
10. Optical properties of the recoil spectrometer for two extreme rays in the horizontal plane: a) medium value for θ_o^r and large value for δ_o^r and b) large value for θ_o^r and $\delta_o^r = 0$. In both cases $y_o^r = \phi_o^r = 0$, and $x_o^r = 0.25$ cm. The curves were calculated with the TRANSPORT model. The solid curves include both first- and second-order matrix elements, while the dashed curves (indistinguishable from the solid curve in plot b) include only first-

order matrix elements. The horizontal solid lines indicate, from left to right, the apertures of magnets Q4, Q5, Q6, B5, B6, B7 and B8.

11. Same as Figure 10 except for rays in the vertical plane: a) medium y_o^r value and large ϕ_o^r and b) large y_o^r value medium ϕ_o^r . In both cases $x_o^r = \theta_o^r = \delta_o^r = 0$.
12. The maximum acceptance angles $(\phi_o^r)_{max}$ and $(\theta_o^r)_{max}$ of the recoil spectrometer as a function of position along the beam axis z_o^r . The target center is at $z_o^r = 0$. The solid lines were calculated using the thin lens model described in the text. The dashed lines show the largest recoil angles dictated by electron-deuteron elastic kinematics for the design values of the electron arm acceptance angles $(\theta_o^e)_{max}$ and $(\phi_o^e)_{max}$. These calculations used formulas (3.6) and (3.7) convoluted with multiple scattering effects.
13. The variation of the recoil spectrometer solid angle with relative momentum δ_o^r for a thin target calculated with the Monte Carlo model.
14. Electron beam intensity profiles at the beam dump: a) projected onto the horizontal axis, and b) projected onto the vertical axis. Two extreme cases are shown corresponding to electron-deuteron kinematics at $Q^2=1$ (GeV/c)² with a 10 cm long target (solid curves) and $Q^2=5$ (GeV/c)² with a 40 cm target (dashed curves). The profiles were generated using the program DECAY TURTLE and include the effects of energy loss and multiple scattering in the targets.
15. a) The ratio of the nominal current I_{ep} of magnet B3 as derived from the electron-proton calibration data to the calculated current I_{cal} versus the momentum p_e' of the electron spectrometer. b) The same ratio for magnet B4. The calculation used the absolute measurement of the integrated magnetic field from the long coil measurements and the shape of the field from the Hall probe measurements.
16. Setup used to measure the vertical focusing of the electron spectrometer. A 1.1 cm thick tungsten shield with circular apertures along the vertical

axis was placed between Q3 and a 0.64 cm thick Al target. Electrons with well defined vertical angles ϕ_o^e passed through the holes to be imaged at specific y^e locations in the wire chambers.

17. Comparison between the optics model of the electron spectrometer and data from the special calibration measurement run with the tungsten shield and the Al target (see Figure 16). The arrows show the predicted positions for the centroids of the peaks.
18. Comparison between data and Monte Carlo prediction for the θ^e electron distribution at the center of the electron arm wire chambers for ep elastic scattering using a 0.937 GeV beam incident on a 10 cm long target. The coordinate θ^e is directly proportional to δ_o^e .
19. Same as Figure 18 except for y^e , which is proportional to ϕ_o^e .
20. Comparison between data and Monte Carlo prediction for the x^r recoil proton distribution at the center of the recoil arm wire chambers for ep elastic scattering using a 0.937 GeV beam incident on a 10 cm long target.
21. Same as Figure 20 except for θ^r .
22. Effective single-arm (squares) and double-arm (circles) solid angles for ep elastic scattering versus target length for a beam energy of 1 GeV calculated with the Monte Carlo program. The geometric single-arm solid angles for $\delta_o = \pm 1\%$ are also shown (diamonds).
23. Double-arm electron-proton elastic cross sections divided by the prediction of the dipole law, compared with backward angle data from previous experiments (CEA, BONN, DESY, Stanford) and forward angle data from SLAC, as compiled in Ref. 17. The NE4 cross sections are averaged over the different target lengths used at each kinematic point.
24. Ratio of single-arm to double-arm electron-proton elastic cross sections as a function of Q^2 , averaged over the different target lengths used at each kinematic point.

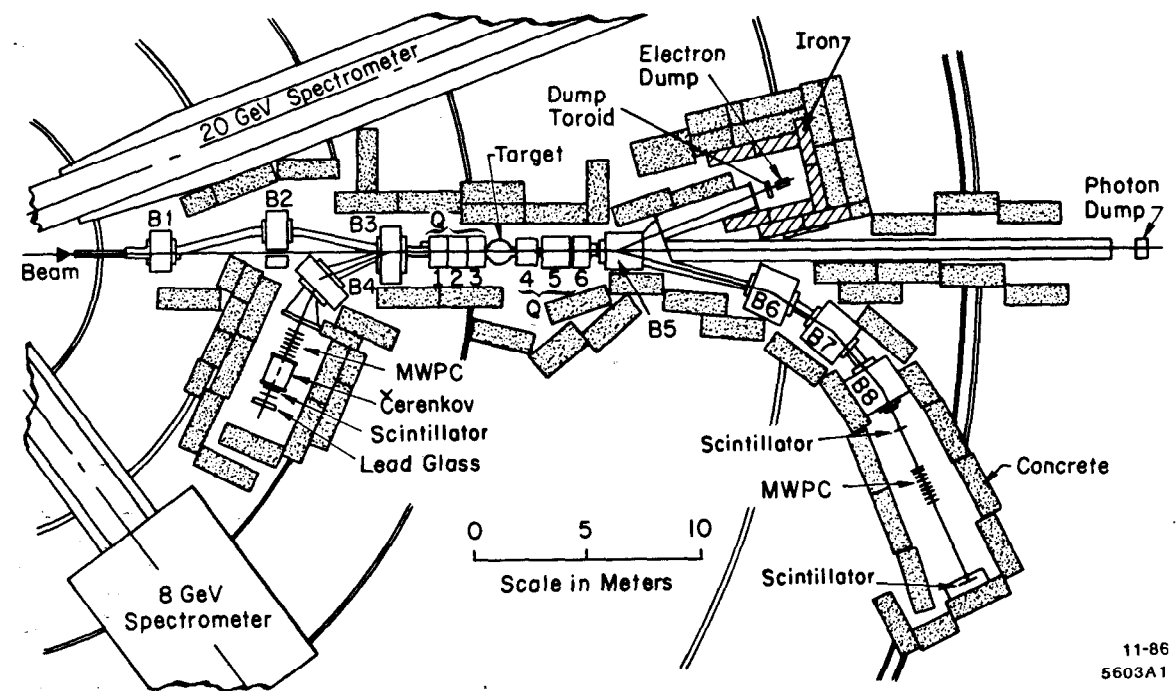


Fig. 1

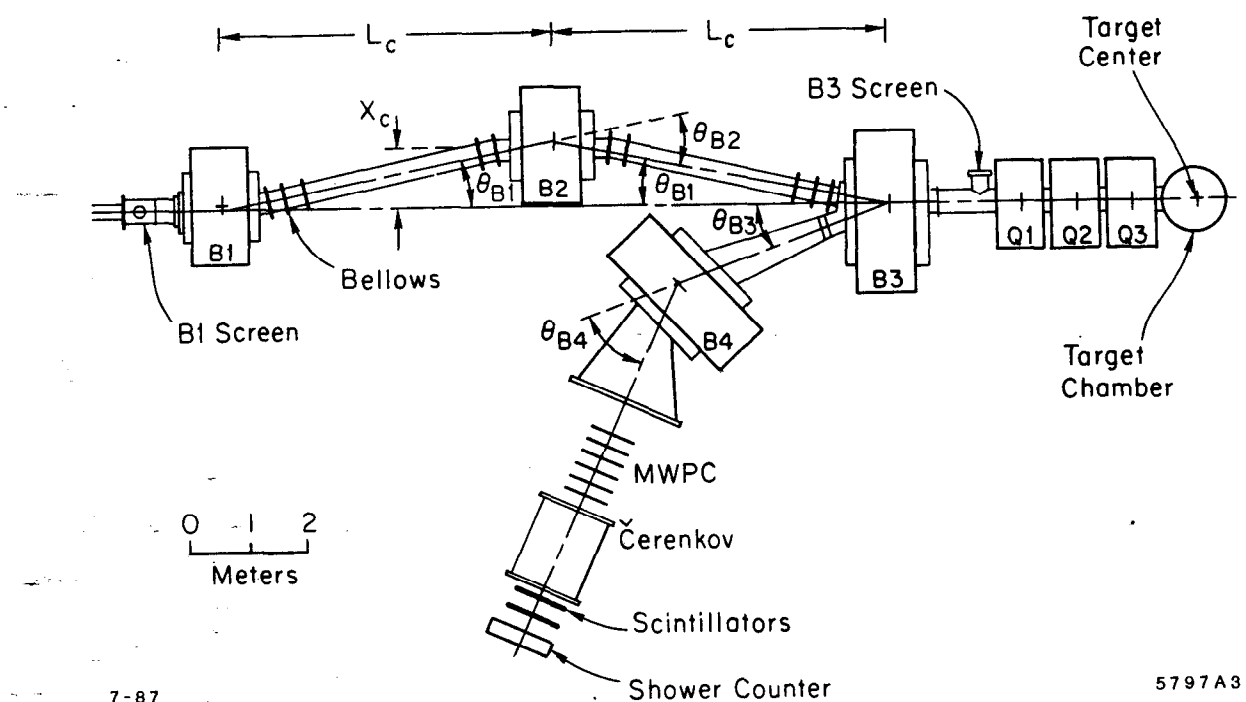


Fig. 2

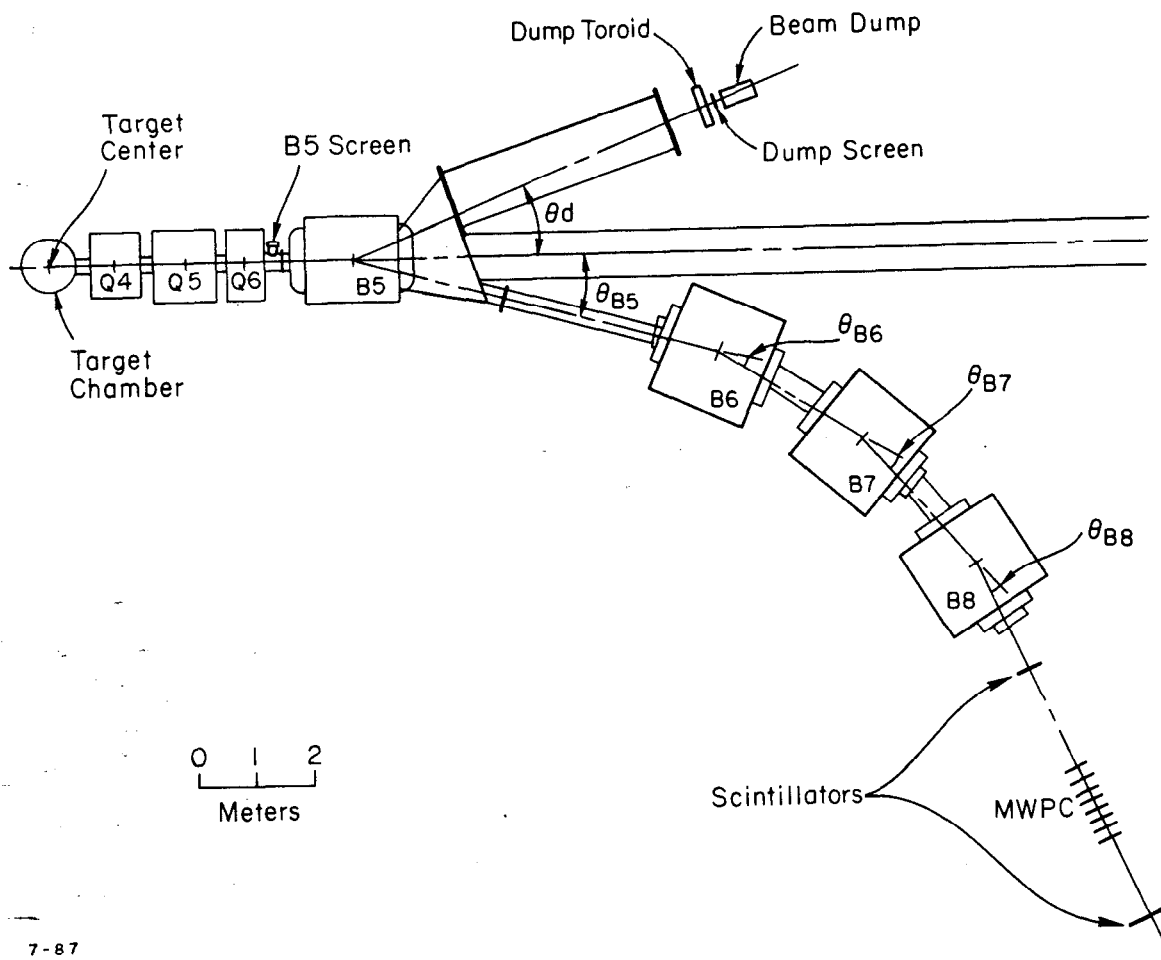
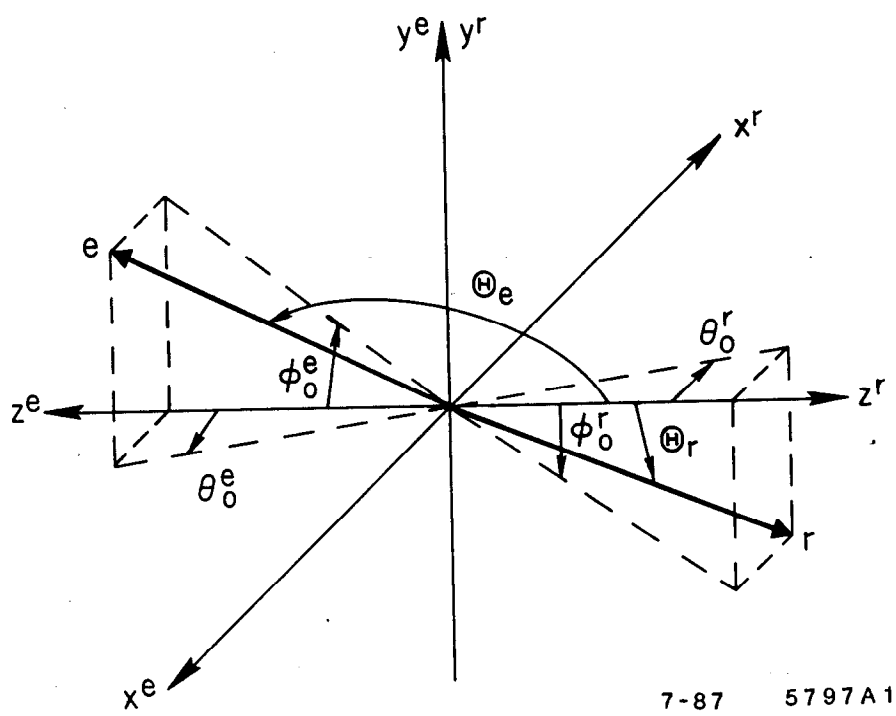
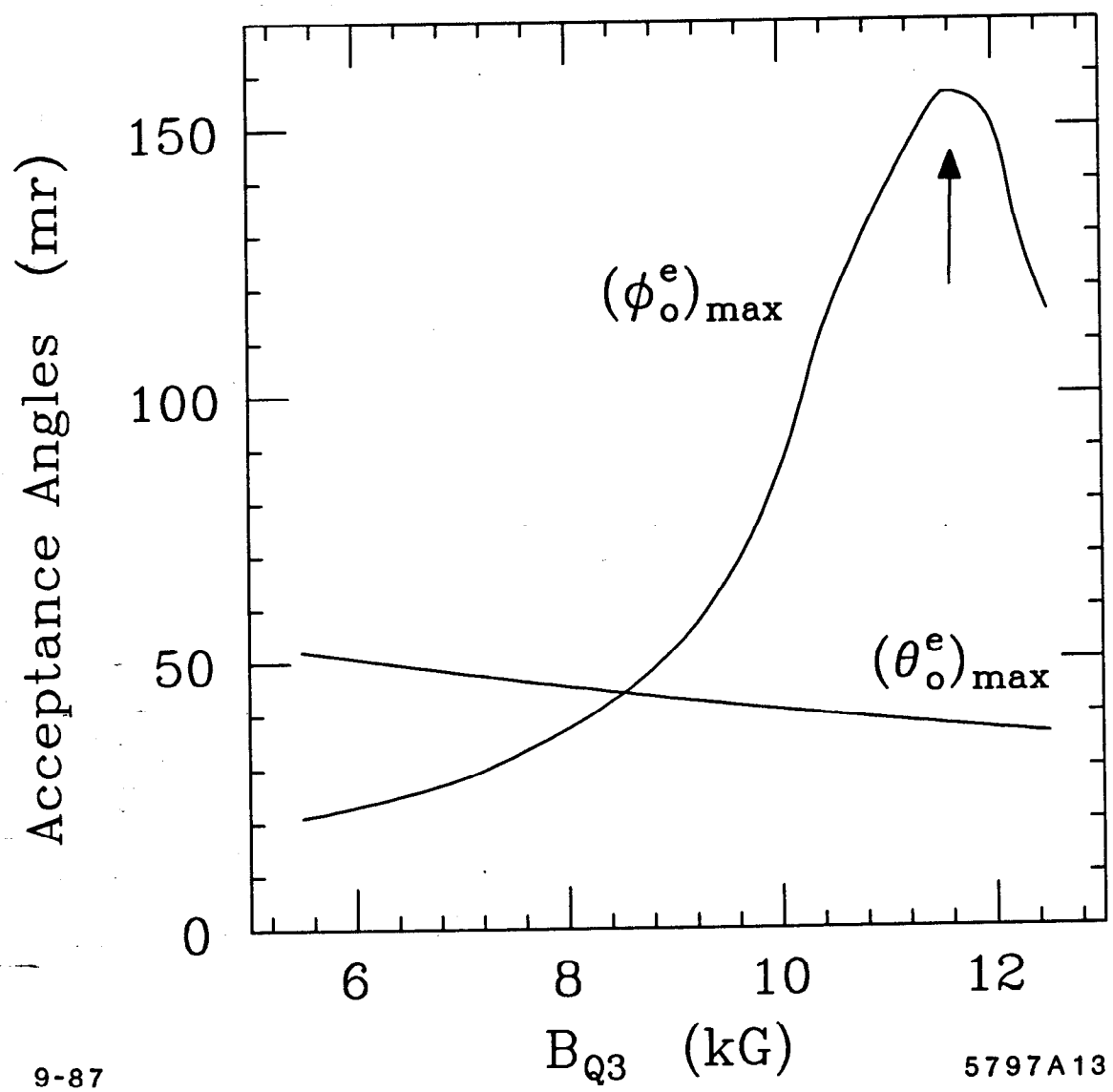


Fig. 3



7-87 5797A1

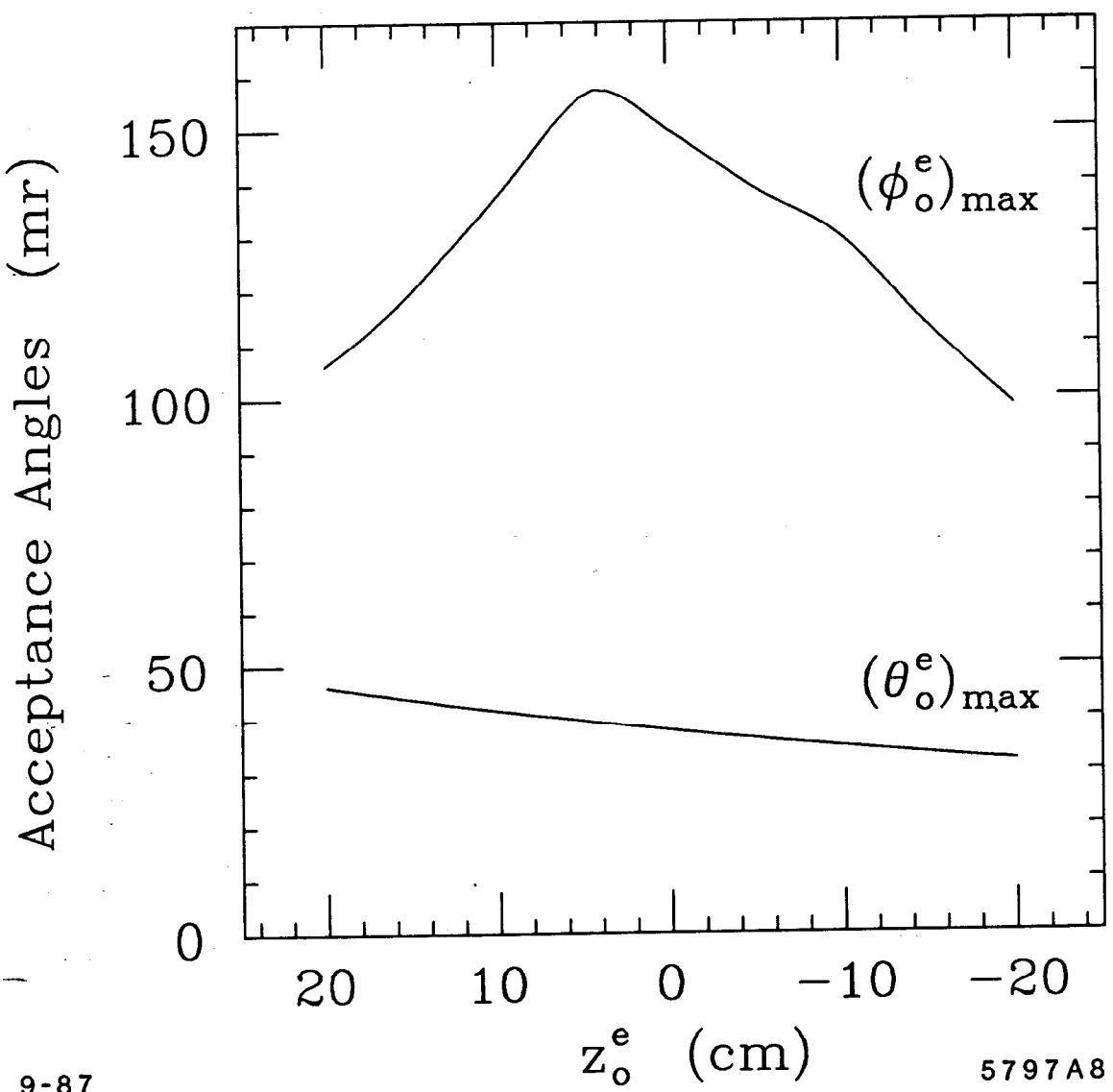
Fig. 4



9-87

5797A13

Fig. 5



9-87

5797A8

Fig. 6

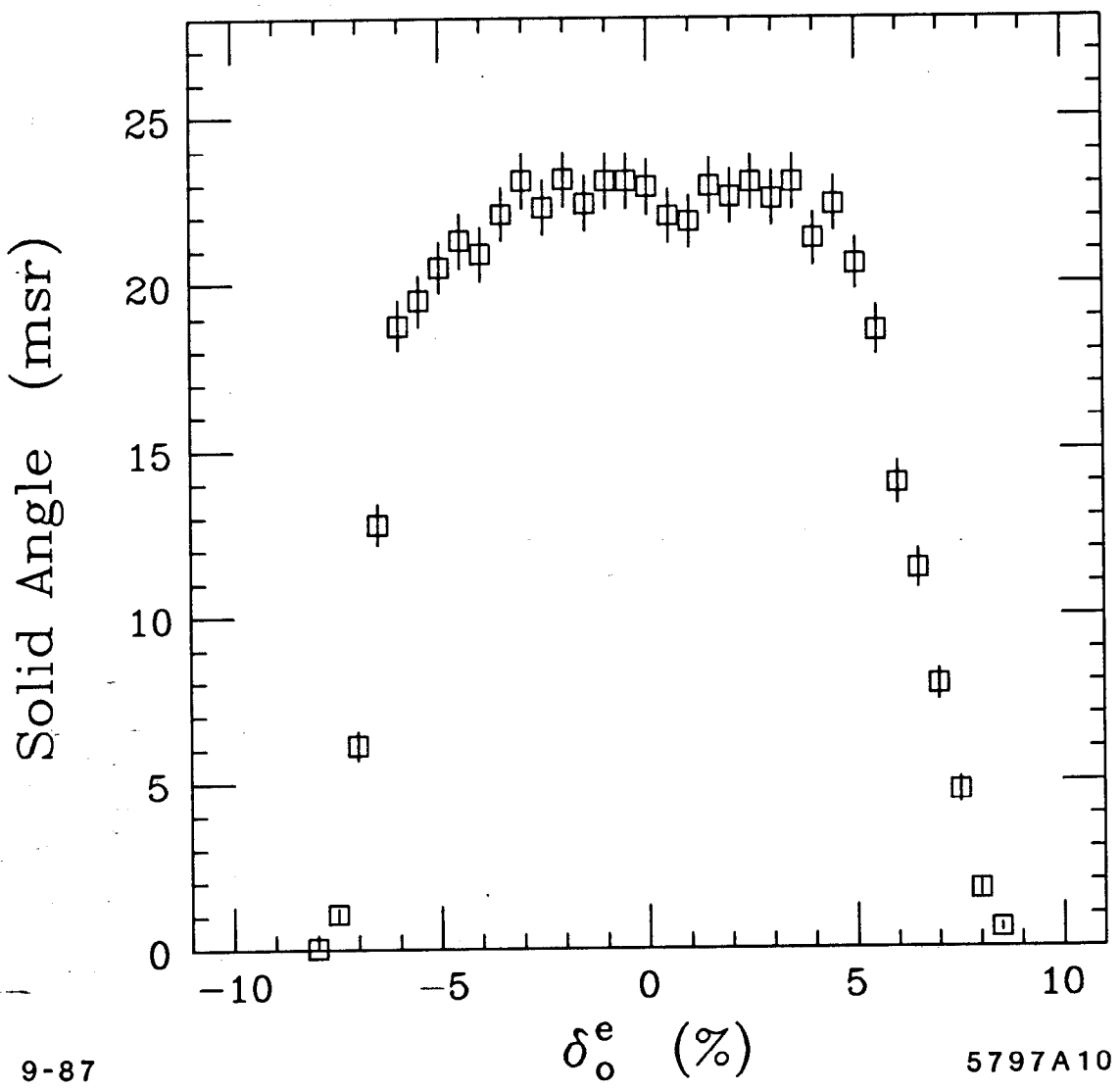
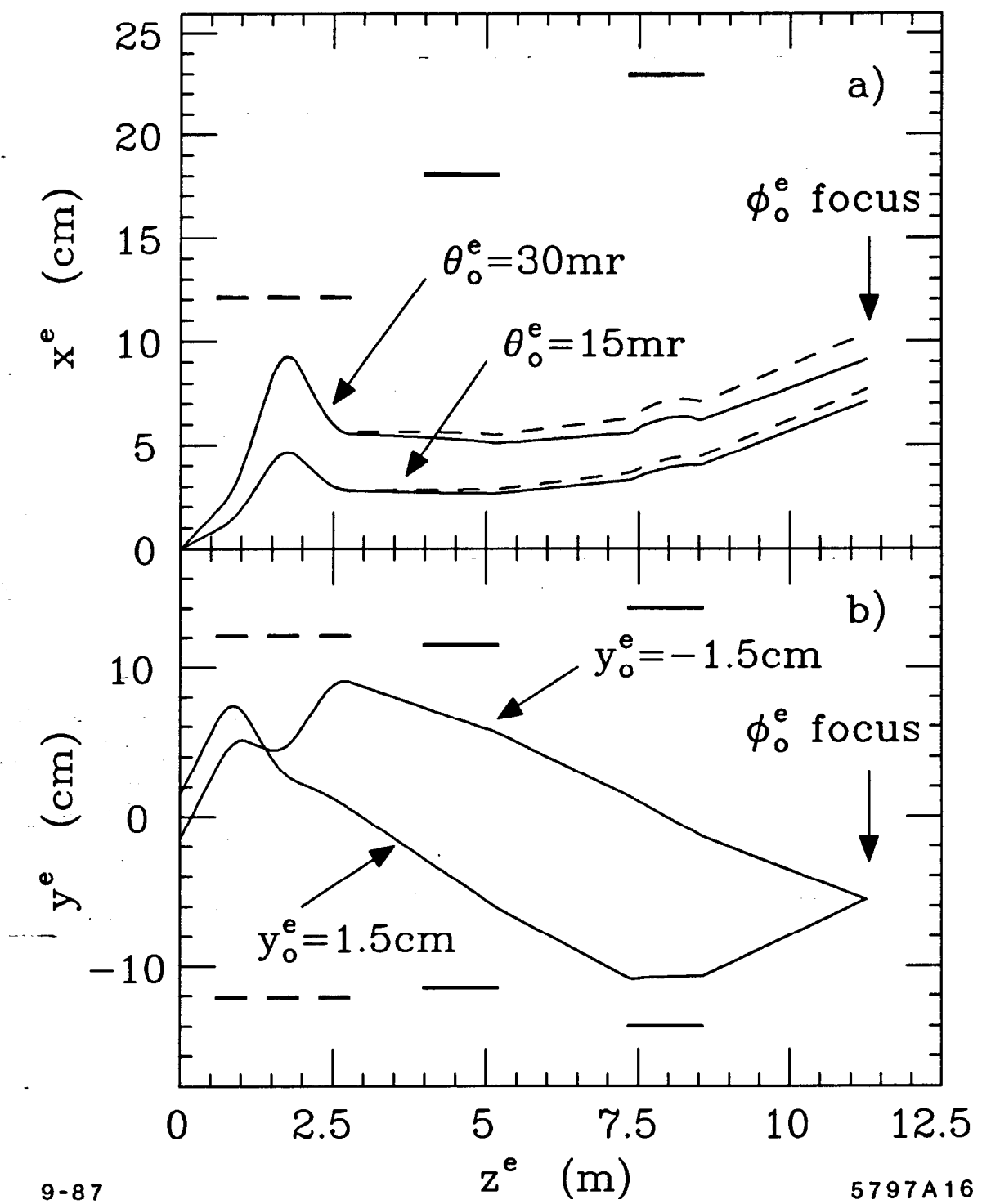


Fig. 7



9-87

5797A16

Fig. 8

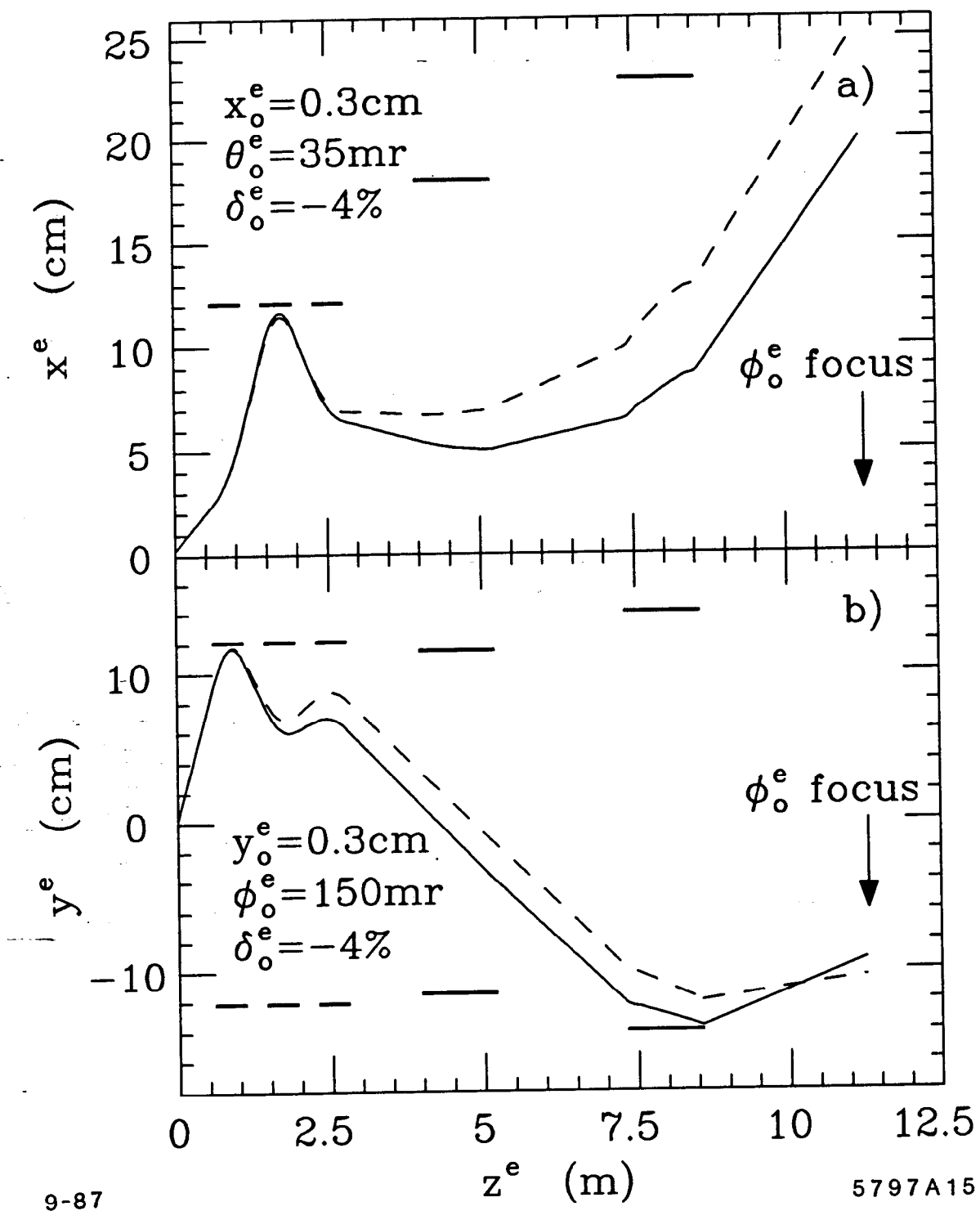


Fig. 9

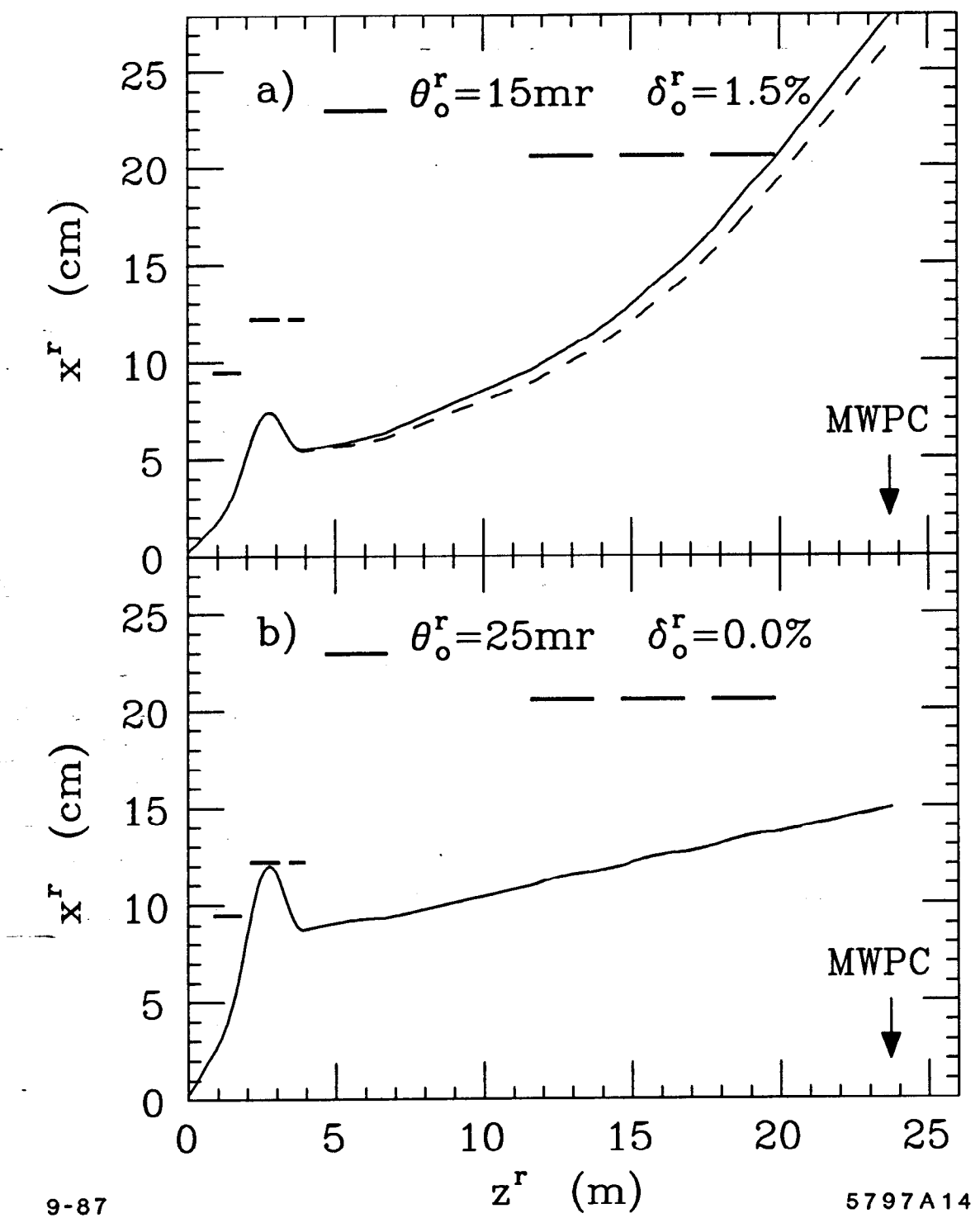


Fig. 10

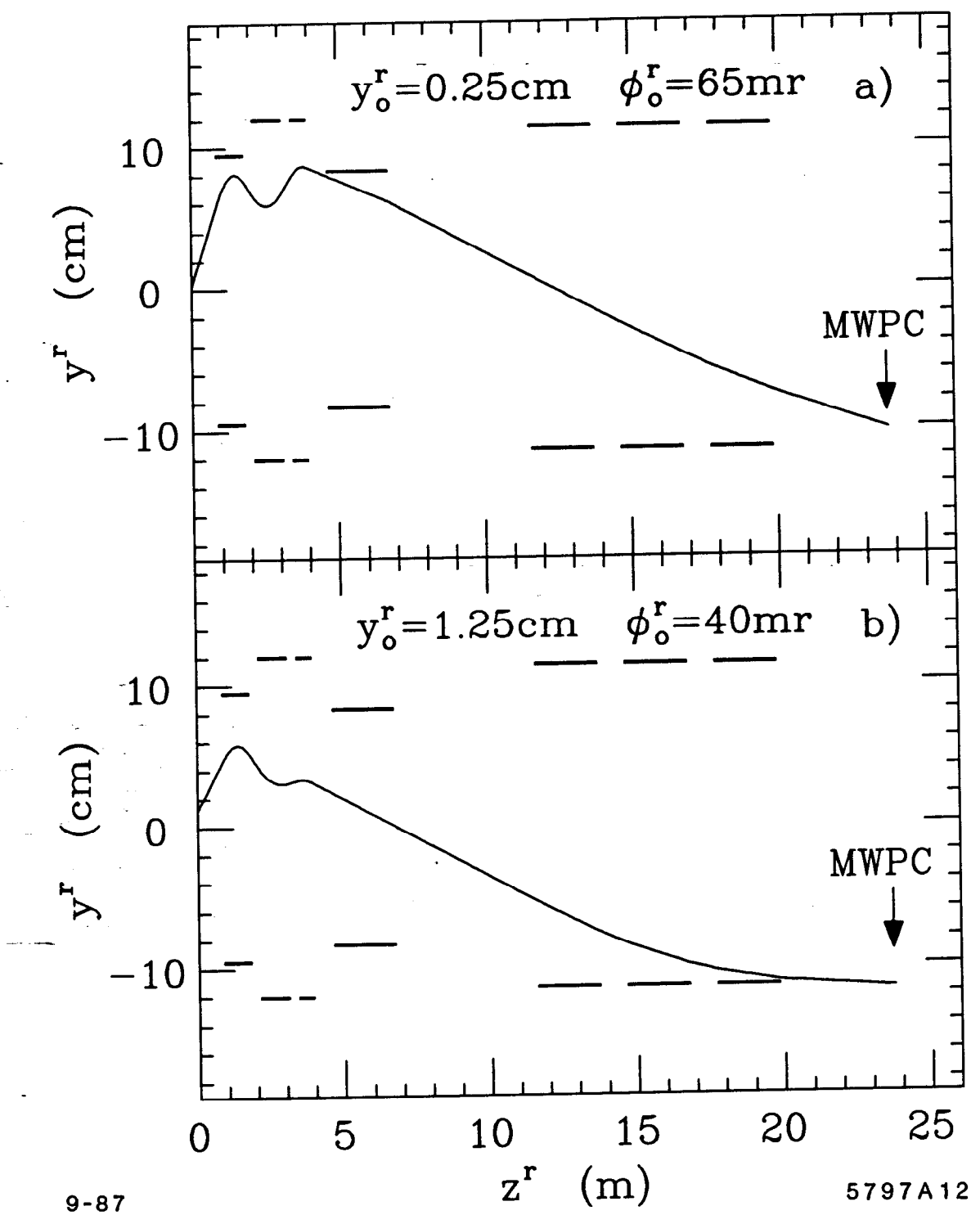
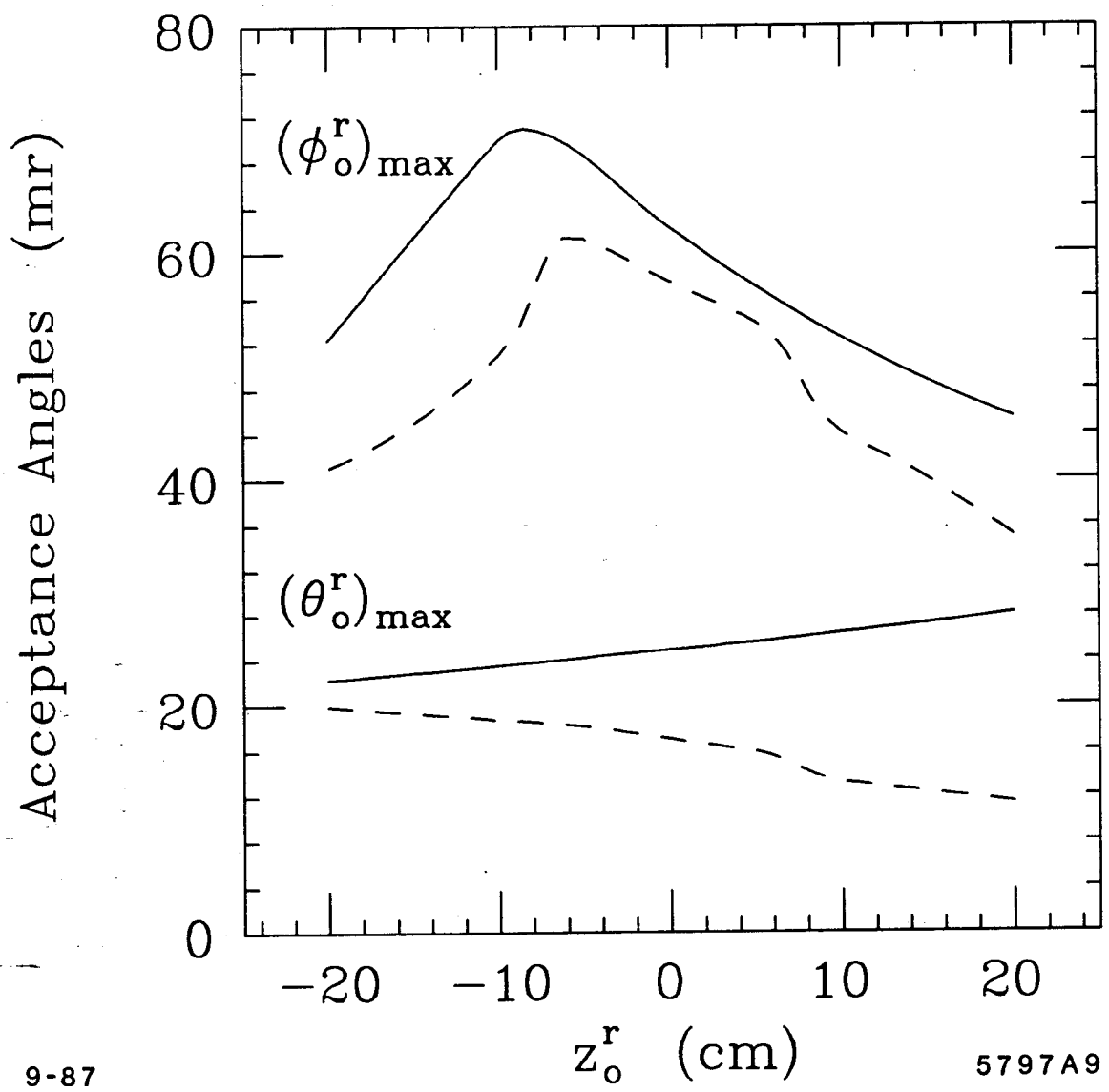


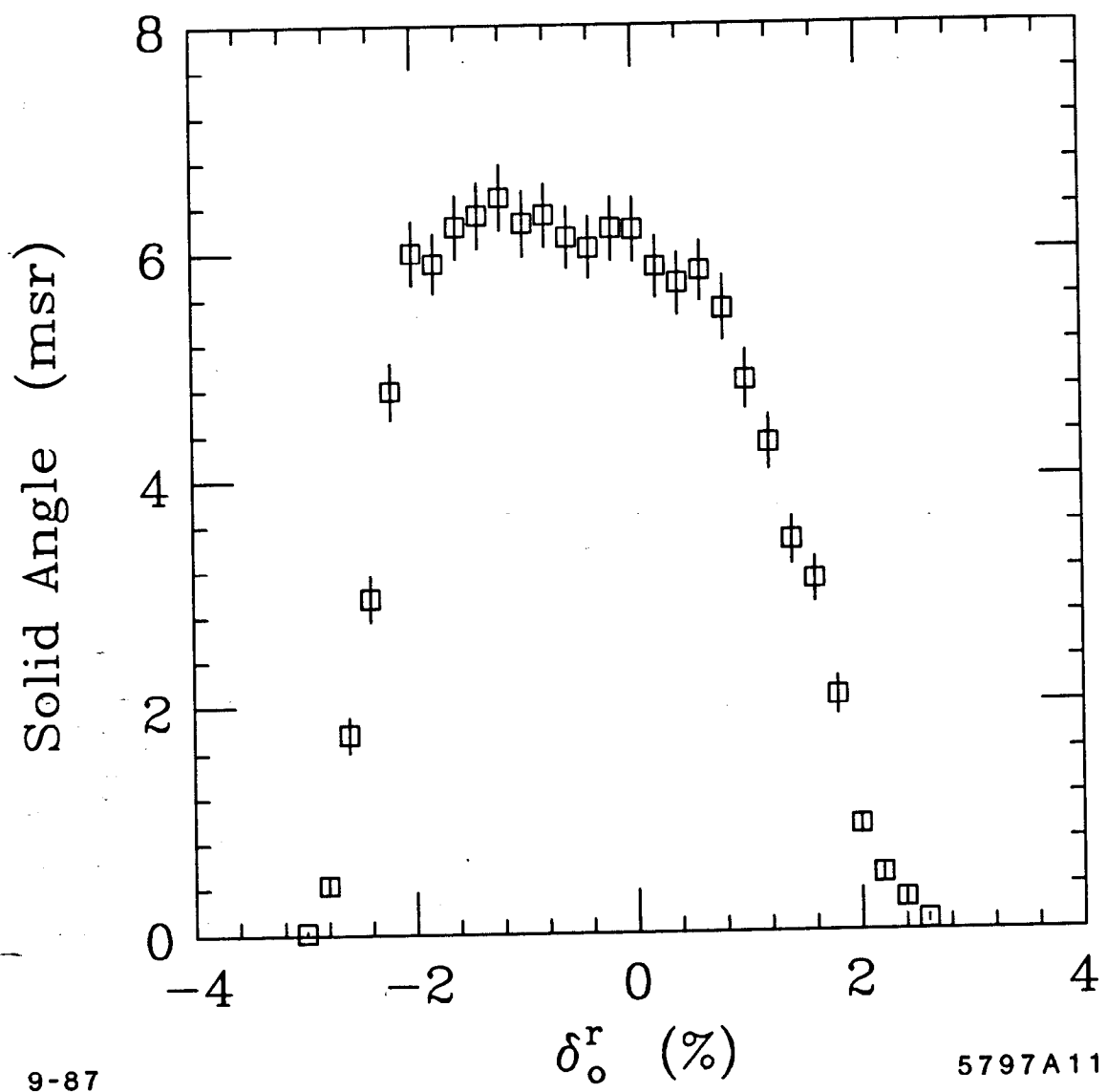
Fig. 11



9-87

5797A9

Fig. 12



9-87

5797A11

Fig. 13

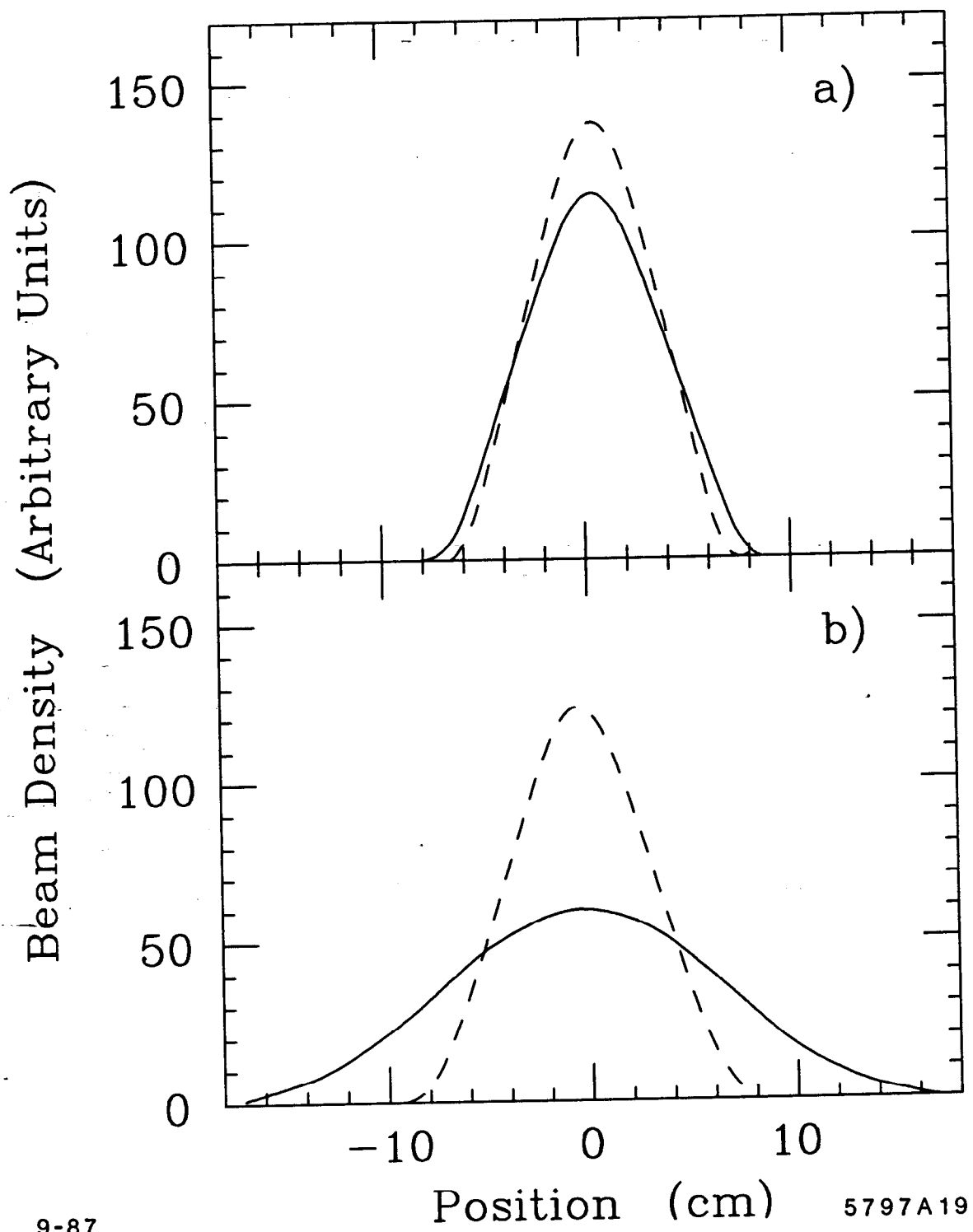
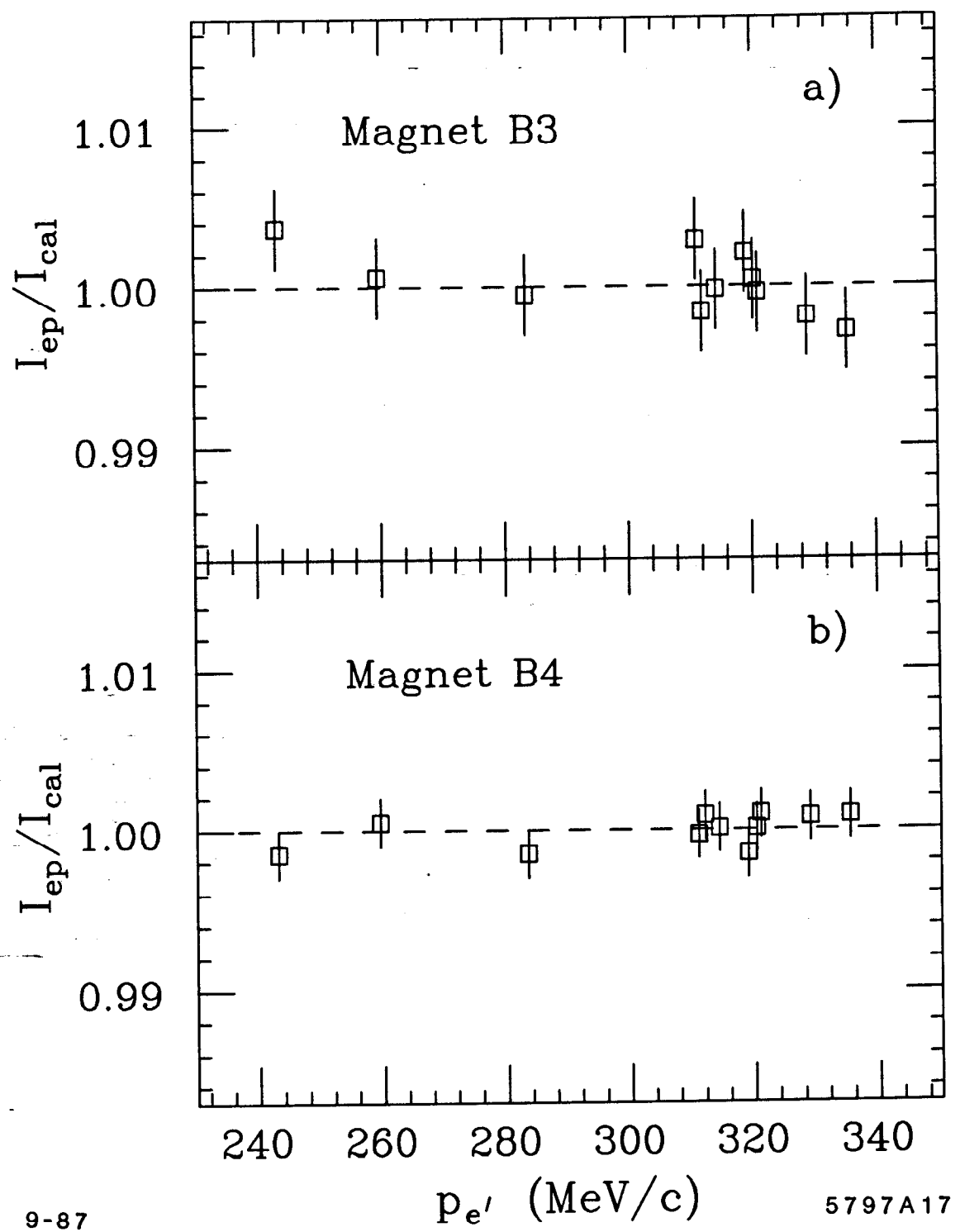


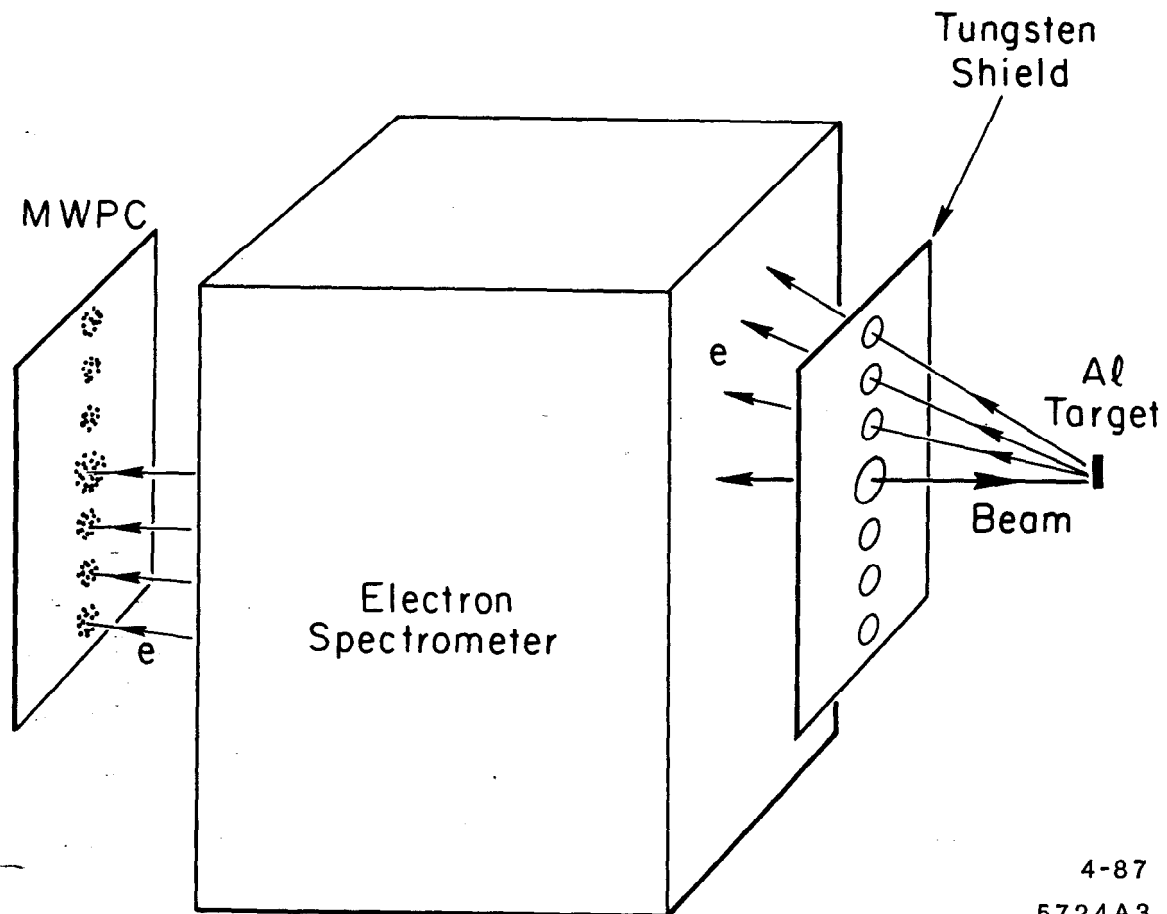
Fig. 14



9-87

5797A17

Fig. 15



4-87
5724A3

Fig. 16

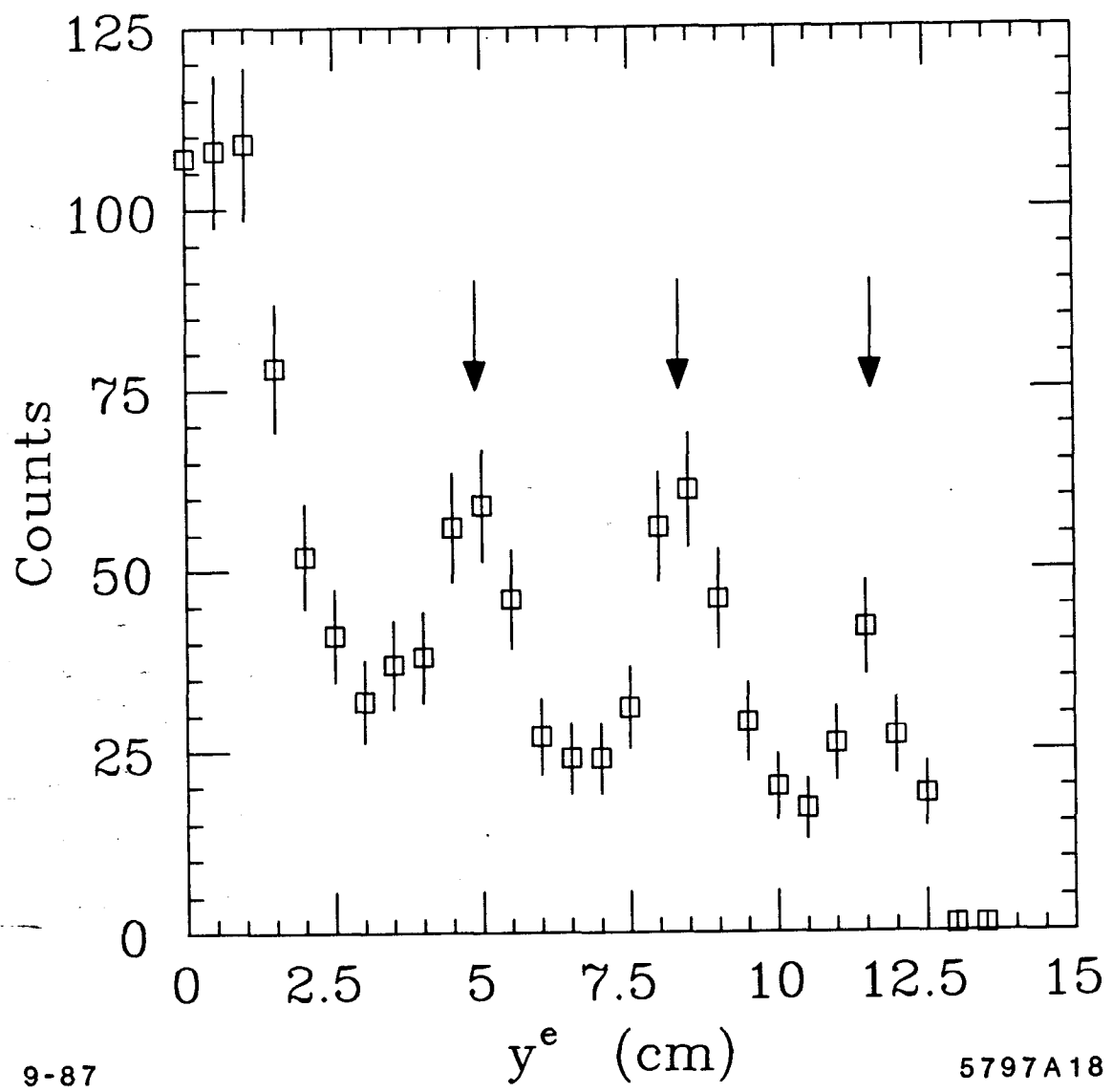


Fig. 17

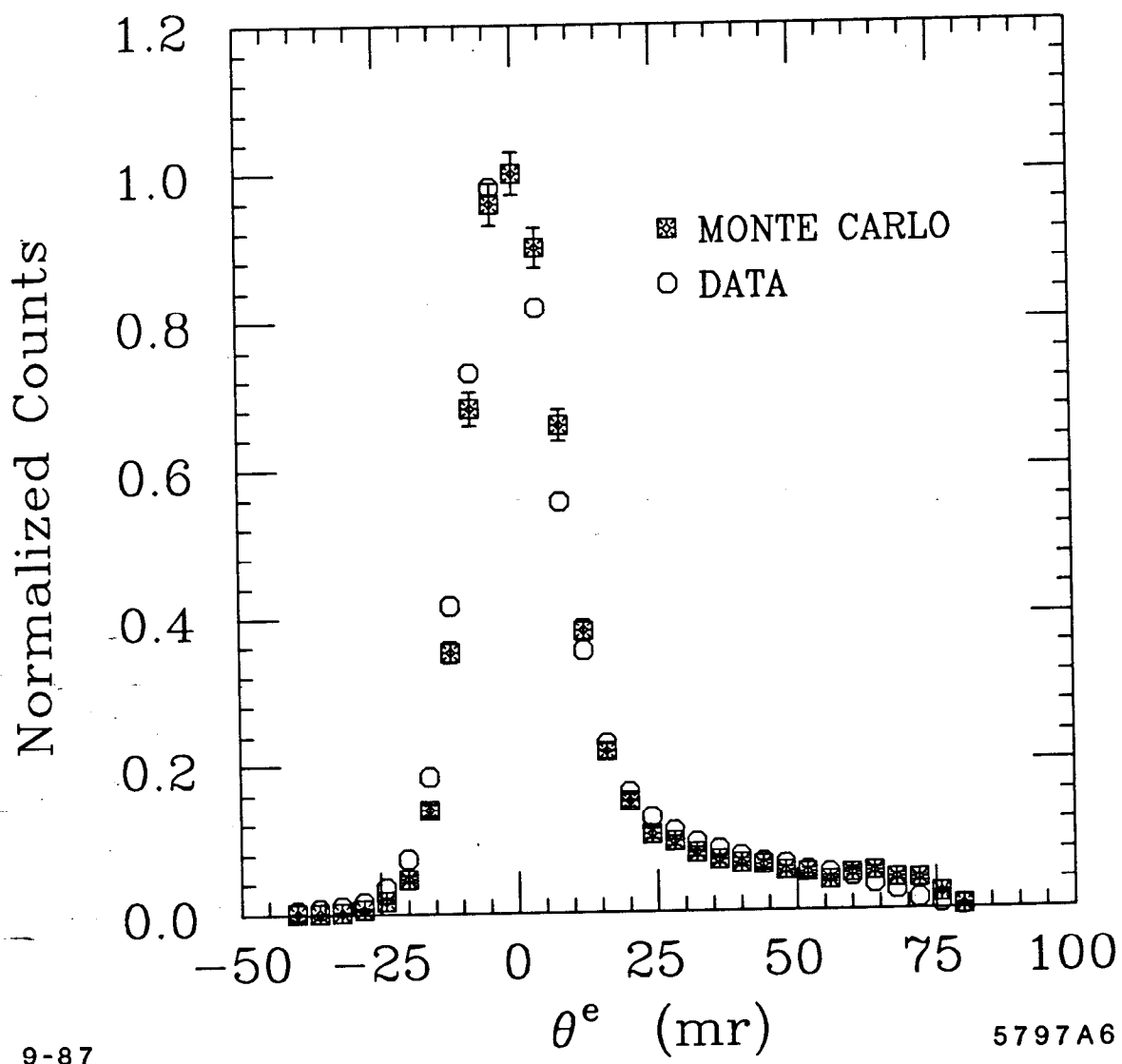


Fig. 18

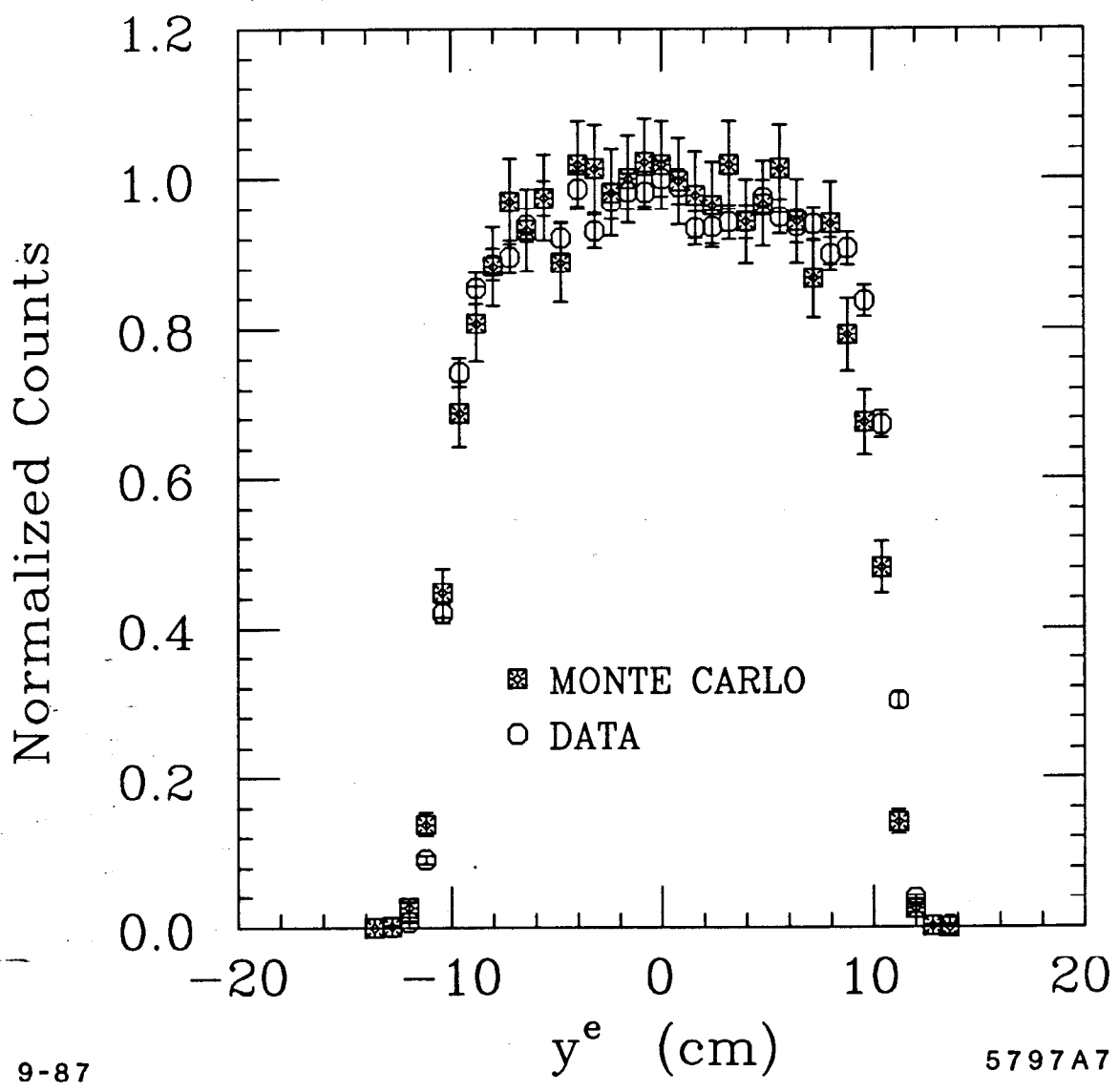


Fig. 19

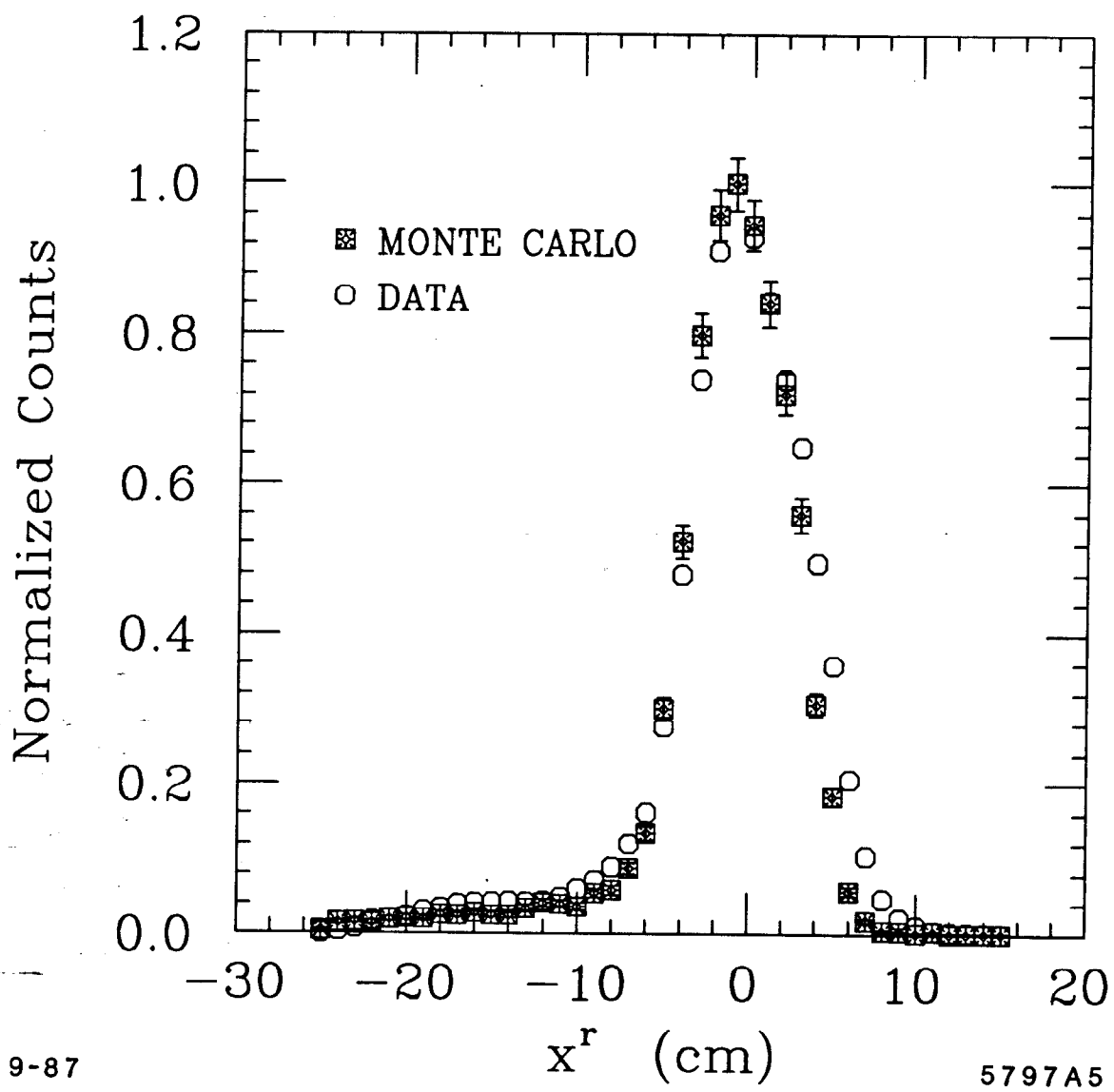


Fig. 20

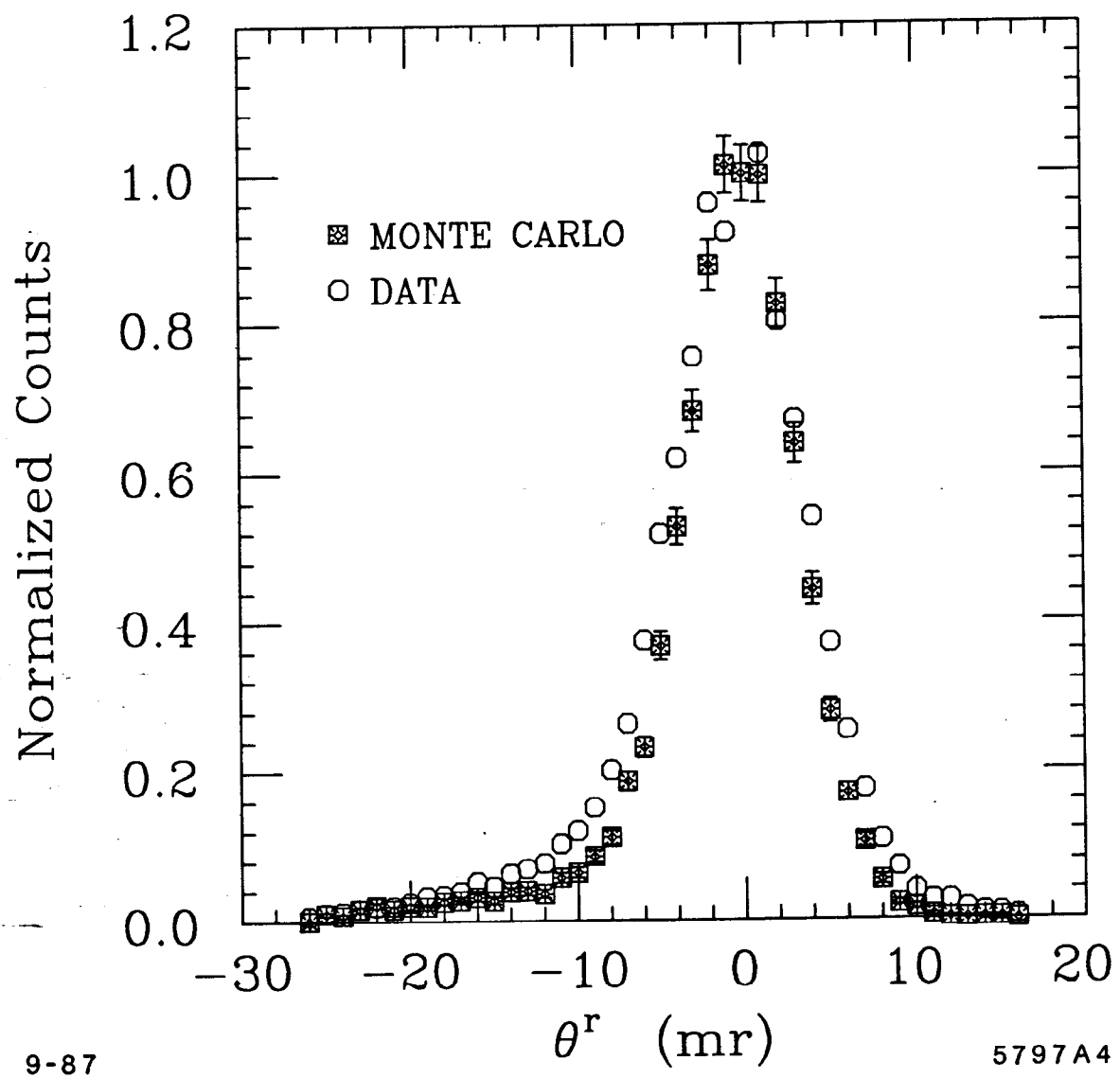


Fig. 21

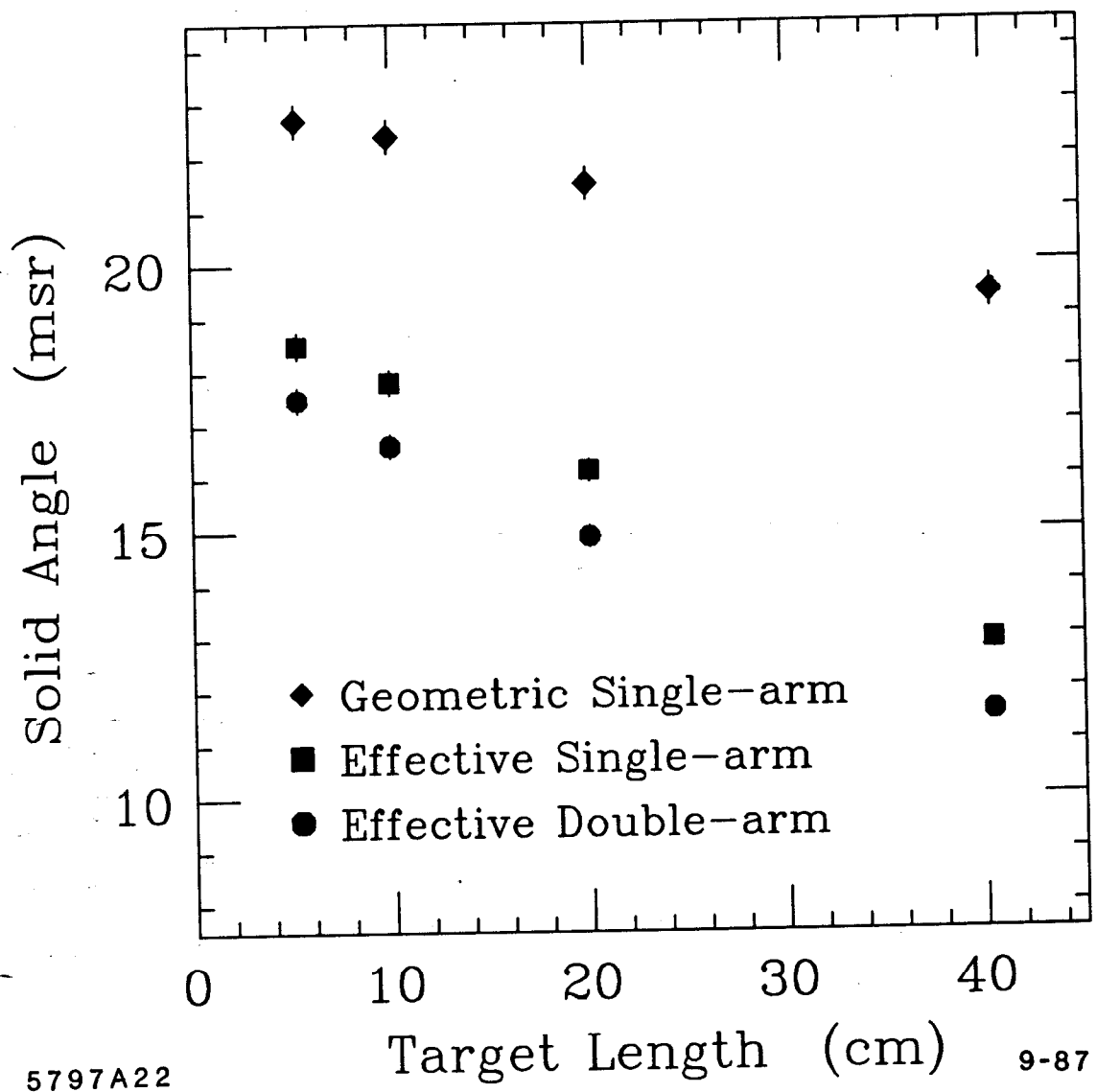


Fig. 22

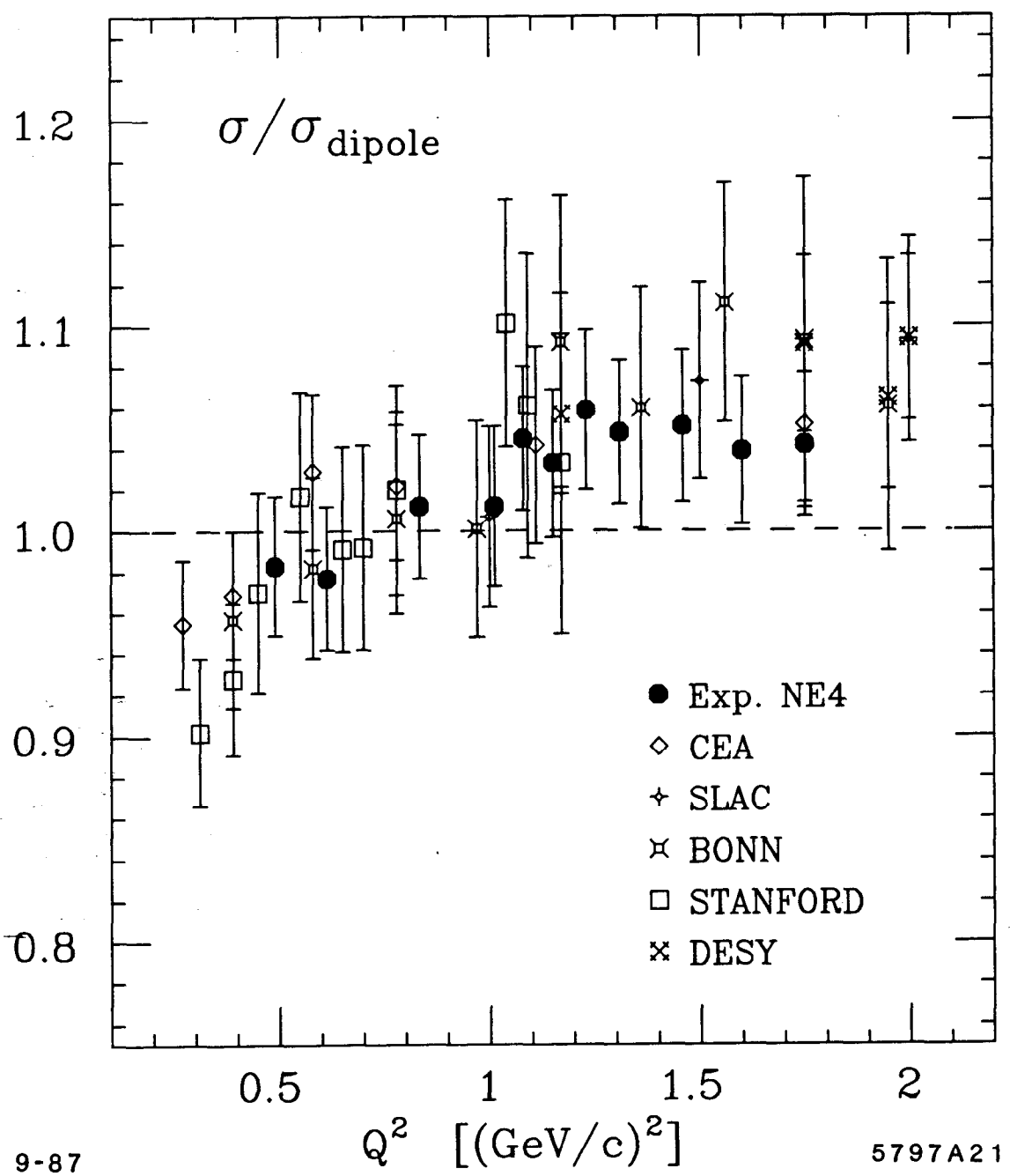


Fig. 23

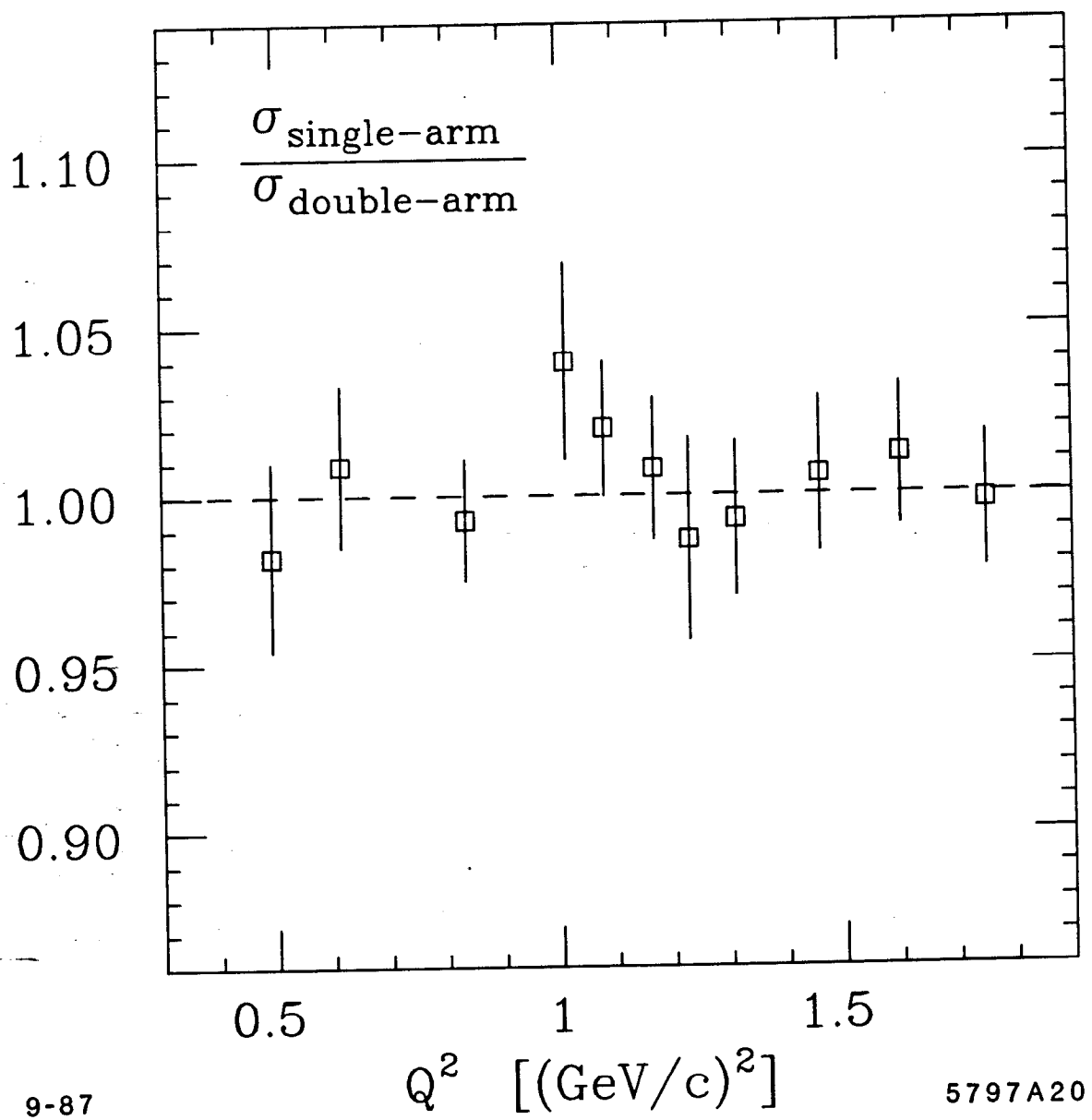


Fig. 24